Wright State University

CORE Scholar

2022

Vibration Bending Fatigue Analysis of Additively Repaired Ti-6Al-4V Airfoil Blades

Lucas Jordan Smith
Wright State University

Follow this and additional works at: https://corescholar.libraries.wright.edu/etd_all

Part of the Mechanical Engineering Commons

Repository Citation

VIBRATION BENDING FATIGUE ANALYSIS OF ADDITIVELY REPAIRED

TI-6AL-4V AIRFOIL BLADES

A thesis submitted in partial fulfillment of the
requirements for the degree of
Master of Science in Mechanical Engineering

By

LUCAS JORDAN SMITH

B.S.M.S.E., Wright State University, 2020

2022

Wright State University

WRIGHT STATE UNIVERSITY

GRADUATE SCHOOL

July 18, 2022

I HEREBY RECOMMEND THAT THE THESIS PREPARED UNDER MY
SUPERVISION BY Lucas Jordan Smith ENTITLED Vibration Bending Fatigue
Analysis of Additively Repaired Ti-6Al-4V Airfoil Blades BE ACCEPTED IN
PARTIAL FULFILLMENT OF THE REQUIREMENTS FOR THE DEGREE OF
Master of Science in Mechanical Engineering.

_____
Joy Gockel, Ph.D.
Thesis Director

_____
Raghavan Srinivasan, Ph.D.,
P.E.
Chair, Mechanical and Materials
Engineering Department

Committee on Final Examination:

_____
Joy Gockel, Ph.D.

_____
Nathan Klingbeil, Ph.D.

_____
Onome Scott-Emuakpor, Ph.D.

_____
Barry Milligan, Ph.D.
Dean of the Graduate School

ABSTRACT

Smith, Lucas Jordan. M.S.M.E., Department of Mechanical and Materials Engineering, Wright State University, 2022. Vibration Bending Fatigue Analysis of Additively Repaired Ti-6Al-4V Airfoil Blades.

Repairing airfoil blades is necessary to extend the life of turbine engines. Directed energy deposition (DED) additive manufacturing (AM) provides the ability to add material at a specific location on an existing component. In this work, AM repairs on Ti-6Al-4V airfoil blades were analyzed to determine what effect the repair will have on the blade performance in high cycle vibration fatigue testing. Targeted sections were cut out of airfoil blades near high stress locations and repaired using DED. To understand the defects that arose with this type of repair, computed tomography imaging was used to quantify the defects from the AM process. The blades were then tested until failure using vibration bending fatigue to simulate turbine engine loading conditions. Results suggest that understanding the impact of internal and surface level defects arising from the AM process is critical towards the implementation of AM repair in aerospace components under fatigue loading.

Contents

List of Figures

List of Tables

1 Introduction

1.1 Overview

Manufacturing, repairing, and replacing expensive parts has always been a concern for any business dealing with the field of aerospace. Finding a more manageable and optimal process for any step has potential to save significant time and money. One area of concern that the field currently struggles with is parts that are damaged in operation and can no longer pass inspection to continue use in the field. Problems such as this have caused many types of machinery to go out of order, which has been shown to potentially cause a back log of repairs and replacements necessary to keep these machines in operation for extended periods of time. A part that has been affected by this specifically is the integrally bladed rotors that are included in many of the modern jet engines used by the military. These rotors made from one piece of material were originally designed for better performance but have shown to be quite the expensive replacements when something goes wrong. Testing and verifying a viable repair process for delicate components such as these has become a top priority for some researchers in aerospace.

Currently, basic repair processes exist that have been approved, but these processes are limited in the amount of damage that can be reversed for a rotor to return to operation. This is due to such complex geometry and potential for severe changes in mechanical performance if a repair is not completed properly. Since there is so much uncertainty around the concept of repairing these rotors, many times the damaged parts are fully replaced with a newly manufactured version that is always very expensive. This leaves the original part useless since the damage is too severe and there is not a repair process good

enough to return it to operation. A repair process that is currently being researched involves using additive manufacturing, also well known as 3D printing, as a way to restore these rotors and many other expensive parts so that expensive replacements will be required much less often.

The field of additive manufacturing has been under strong development for many years but has seemed to gather a lot of traction in the last decade. More complex parts and applications are being created that heavily benefit from the use of additive manufacturing and the advantages that it provides. Using AM to repair expensive aerospace parts such as IBRs would create more time and resources for research and development of improving the current machinery during the creation of successors instead of needing to waste it on fixing the current broken pieces piling up from minimal damages. Overall, finding a way to use AM for repairs could open up a lot of opportunities for both aerospace manufacturing and the field of additive repair.

1.2 Contributions

The contributions of this thesis are as follows:

1. Investigates the effectiveness of directed energy deposition additive manufacturing repair techniques for integrally bladed rotors under vibration fatigue loading

2. Examines the formation and detection of defects in additive repairs using computed tomography scans and image processing techniques

3. Compares the results from vibration fatigue testing of two types of directed energy deposition additive manufacturing processes used to repair turbine engine airfoil blades

4. Studies the prediction of fatigue life based on porosity size and location relative to mode two bending stress distribution

2 Literature Review

2.1 Integrally Bladed Rotors

Modern jet engine rotors, referred to as blisks or Integrally Bladed Rotors (IBRs), have attached blades. These rotors get the designation of IBR since the blades are attached to the hub of the rotor as one solid piece of material, as shown in Figure 1. During operation in an engine, these rotors are spinning and vibrating at high frequency ranges, causing the blades to sometimes encounter multiple modes of bending. Each mode of vibration has an associated resonant frequency. This frequency is representative of the number of vibrations per second required for the blade to bend at each mode. There is an increased stress and strain that occurs when the blades vibrate at the resonant frequency that a given blade may have for the different modes of vibration. The blades on these blisks eventually experience failure, such as cracking, due to the high stress that is endured over long periods of use. When a blade becomes damaged, either a repair or replacement is required, but traditional rotor repair can take significant amount of time depending on the complexity of the damage and the number of parts that are experiencing the same type of problems.
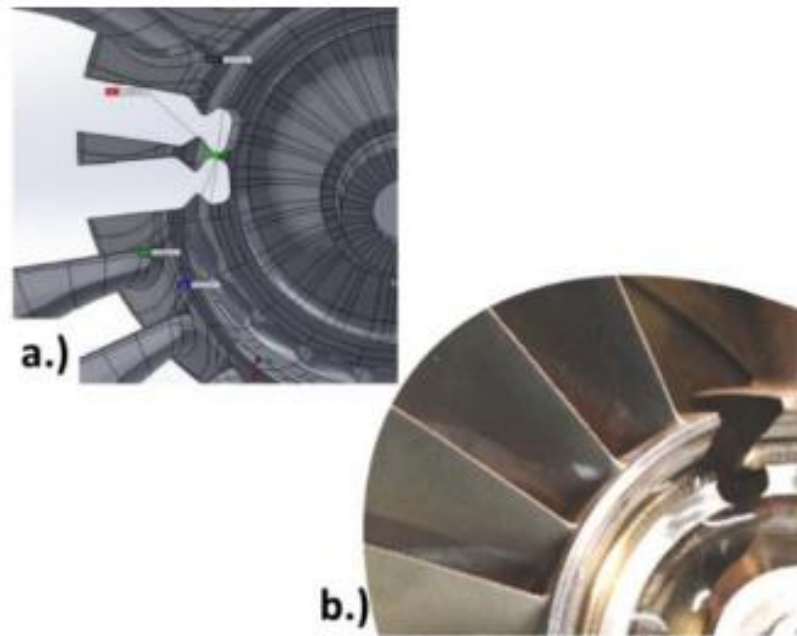
Figure 1: IBR examples with blades being attached to the hub as one large part. [1]

2.2 Current Solutions to IBR Failure

Repairing an IBR is expensive due to the large amount of time and money needed to get the part back in operation. The time and cost are a result from the rotor needing to be sent back to the manufacturer for the proper fix to be determined and implemented. Depending on the issue and the number of failures of a certain component, traditional rotor repair can take a significant amount of time due to the complexity of the damage that has taken place and the number of parts that are experiencing the same type of problems. In many cases, the damage to an IBR is significant enough to require a full replacement which becomes very costly to the owner.

The current repairs that can be done on an IBR are mostly located in low-stress areas of the blade. Low-stress is safer because there is not as much of a risk for when mistakes in the repair process occur since that region of the blade is not experiencing as

much strain as other regions may be. Currently, repairs for these low-stress regions include tip repairs using material cladding with a laser welding technique, crack repairs using either brazing or welding depending on the size of the crack, and patch repairs that weld chunks of material onto the blade in areas where the blade may have been removed. These types of repairs can be seen in Figure 2.
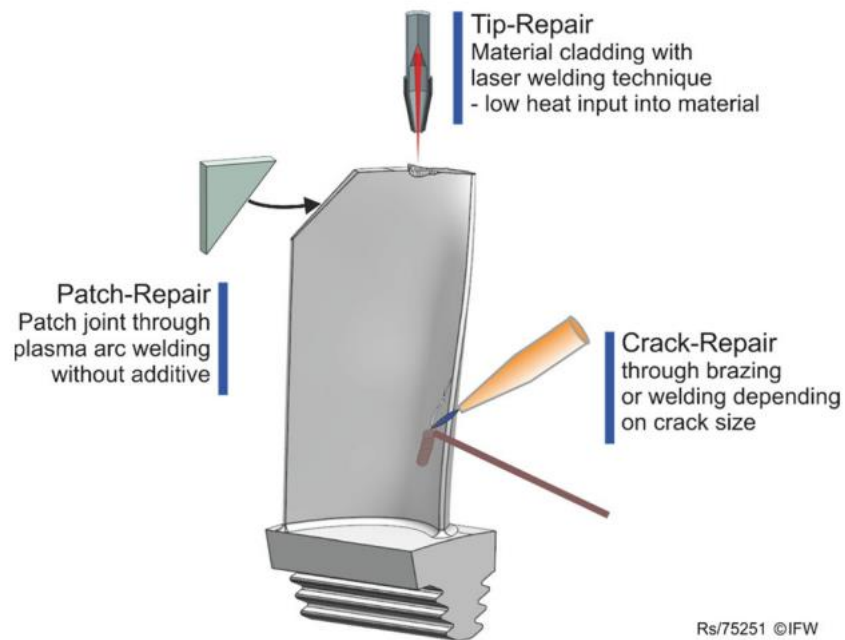
Figure 2: Examples of the current types of repairs that can be done for IBRs [2]

Avoiding repairs in high stress locations means that a full replacement is necessary when this type of damage occurs. Since the blades go through such a vigorous operational life, it is not uncommon for the damage to take place in a high stress location, such as the root of the blade. This full rotor replacement has potential to become a large problem in a small amount of time, especially if the type of failure is common among lots of IBR components that are actively in use, leaving many aircrafts operational until the back log

of replacements can be completed. This still leaves the broken IBRs useless, however, but there may be a way to salvage these expensive components.

2.3 IBR Repair Using AM

Directly repairing blades via additive manufacturing (AM) has potential to save time and money because it can be completed directly on the blade without removing it from the configuration or causing further damage to the rest of the component. As mentioned previously, the current repair techniques are unable to repair highs tress areas on blades that are part of an IBR. With AM, these areas of damage can be more effectively repaired and return to operation. This can be done without needing to replace the blades or the rotor, it is much cheaper than traditional means of repair, and the process saves a significant amount of time [3]. Research has been moving towards finding a reliable form of AM repair for these types of components that can be safely implemented in the near future for more efficient repair of expensive aircraft components.

2.4 Additive Manufacturing

Additive manufacturing (AM), also known as 3D printing, is a form of manufacturing that builds on a substrate in layers of material that are added one at a time. This manufacturing process has many different types and forms, as shown in Figure 3. There are six main types of AM: material jetting, material extrusion, direct energy deposition, vat polymerization, powder bed fusion, and binder jetting. Most forms of AM fall into one of these main category types. The goal of each of these AM techniques is to create a part by adding material to form a model. The blueprint for building an AM part comes from a 3D geometry file that can be made in many different types of computer aided

design (CAD) software, such as SolidWorks. The AM machine will read these 3D geometry files and make a print that correlates to the desired part as closely as possible. Some processes are more precise than others, but every AM technique has advantages and disadvantages.
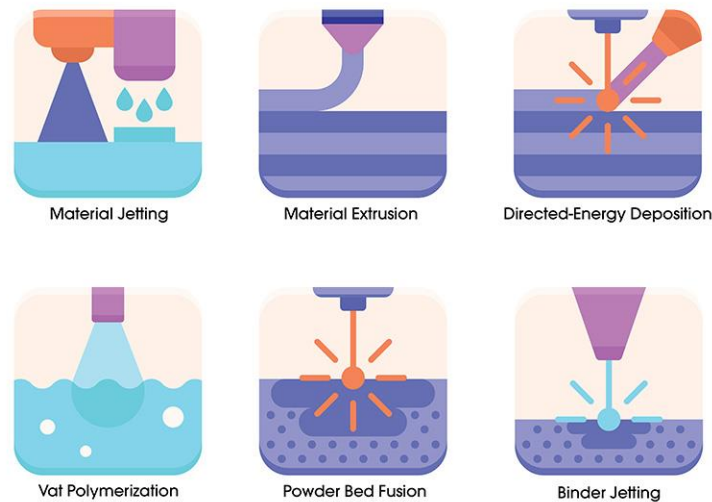
Figure 3: the different types of AM that are common today. [4]

For the topic of repairing a part that already exists, there are few AM options to choose from. The restrictions on some processes have to do with the way the added material needs to bond with the surface and the size limitations of the build chamber in which the repair would need to take place. A technique well suited for blade repair is directed energy deposition (DED). DED has been used to make repairs to components from a multitude of manufacturing and research fields, expanding from repairs on molds [5] and dies [6] to repairs on crankshafts [7] and driveshafts [8]. Repairs using DED have also been used in the field of aerospace to study the effectiveness of the process when being integrated as a tool to remanufacture IBR blades [9].

2.5 Directed Energy Deposition AM

The purpose of this project was to find a process that will work for this type of repair and analyze the ability for it to be used safely and consistently. The technique that was chosen to complete blade repairs is commonly referred to as directed energy deposition (DED), but is similar to brazing, electron beam welding, wire and arc AM, and laser engineered net shaping (LENS™) [10-13] This process feeds metal alloy powder into a laser path that is then melted onto the component in layers [14-15]. These layers can fill large gaps in a component to complete a repair if the area is accessible to the laser [10]. DED processing parameters involve adjusting the feed rate of the metal alloy, as well as the speed the laser moves, and the power of the laser being used to melt the material. Small changes to any of these parameters can have significant impact on the quality of the final build. Figure 4 shows an image of what a powder fed DED process looks like during the building process.

Figure 4: Directed energy deposition using blown powder as the feed source for the metal alloy. [11]

2.6 Challenges of using AM for Repair

Currently, there is significant time and resources being put into the world of AM in an attempt to eliminate all the unknowns of the processes. Solving these unavoidable issues opens significantly more applications that would be able to utilize AM technology. Before this begins to happen, however, there are changes that need to be made. As it stands, there are very few industry standards for the AM processes and processing parameters that create a wide range different outcomes (LEIN, Opportunities and Challenges of Additive Manufacturing in the DoD). When looking at AM for repair procedures on parts such as IBR blades from an aircraft engine, these inconsistencies begin to create a lot of doubt when it comes to dependability. When a repair is required, it is usually due to some sort of damage that has occurred to a part in some fashion. This part now has a defect that can prevent further operation until a fix is provided. If an AM process aimed to repair the defect is only continuing to add more defects during the process, then this repair is not an acceptable procedure for getting the part back into operation. Therefore, a lot of focus in additive manufacturing is trying to find the correct processing parameters and what effects each step of the process truly has on the creation of defects in the build.

The DED AM process is the focus of this work for being used as a repair technique. Since this process has not been perfected, there are still different types of voids that can be found in the builds that are produced using this technique. The main types of pores that are typically observed for DED processes would be gas pores, keyhole pores, and lack of fusion pores (LOF) [12]. DED processes are prone to gas pore formation when the melted alloy rapidly cools after the laser passes through, causing gas bubbles up to 100 µm in diameter to be trapped in the deposited material [13]. Trying to remove these pores after

10

the build is completed is not very effective since the material is completely solidified. Preventing these gas pores during the build would be the best way of eliminating the pores altogether, but this has not been fully accomplished yet.

The most detrimental type of pores that is found in the DED process is LOF, which can be seen in an x-ray image of a repaired blade in Figure 5. These occur when there is either not enough feed material being put into the laser path, or not enough energy being applied between the power of the laser and the speed at which it moves. Both problems give long, thin cavities in the material that usually fall between the layers. LOF pores in DED have been seen at sizes from 200 µm to over 5 mm. Defects of this size will create serious performance issues, especially in a fatigue environment of a highly complex part. The last type of pore that is typically found in DED is a keyhole defect. Keyhole pores can form in the opposite way of LOF, when the laser is either moving too slowly or at a power level that is too high (Stokes, A Route for Avoiding Defects During Additive Manufacturing) [14]. The high energy of the laser can cause a large cavity to form in the melted material. The end of this cavity breaks off at the bottom as the melted material above it reforms and cools from the top down, thus entrapping the void that was previously attached to the cavity. Depending on the laser energy, these pores can become quite large, and are typically larger than the gas pores that can be found in DED builds.
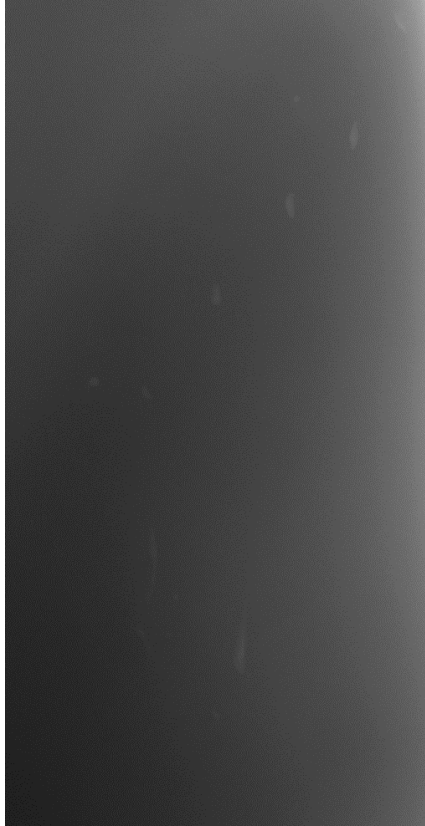
2.7 Non-Destructive Evaluation

To determine whether the AM repair process is successful, computed tomography (CT) can be used as a non-destructive evaluation (NDE) technique to analyze internal pores in the repaired sections on the blades [21, 22]. CT scans use X-rays to capture images of a component in full 360 degree rotation and compile the images using processing software to create a stack of two dimensional cross sections through the entire scan area. Scanning the repaired sections of the blades with X-rays creates a three dimensional volume of the entity that can display pores at the sub-100 µm level [15]. Since AM remains as a field that requires a significant amount of research and development, CT analysis is valuable in exploring the unknown effects of processing parameters on the performance of a specimen

[16]. Characterizing the pores in an AM part before testing procedures occur gives insight to information that would otherwise be completely unknown until the testing was concluded [17]. For traditional means of manufacturing, CT scanning the parts would not be as advantageous, but for AM parts it has proven to be very useful in understanding the benefits, and consequences, of using AM for repairs [18].

Figure 6: Crack found using FPI on a vibration fatigue specimen
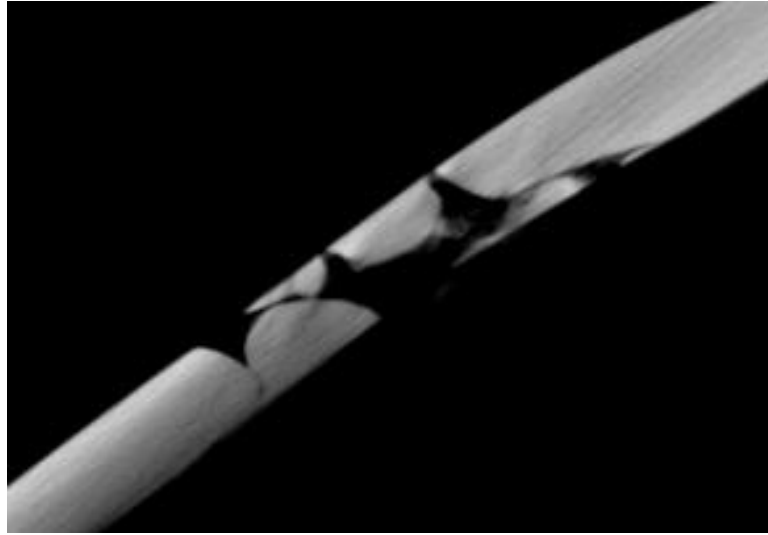
Figure 7: Large lack of fusion pore found in an image generated using CT scanning

2.8 Fatigue Life Prediction

Data collection and analysis of the pores found in the repairs was compiled into a pore distribution process that showed which repair process was more effective and consistent. The CT information was used in tandem with the results from a vibration testing method that represented the stresses a blade of this type would experience during second bend mode while operating in an engine [19]. Grouping these data sets together allowed for Stress Intensity Factor (SIF) calculations that established a better understanding of the causes of failure in some of the repairs that cracked away from the typical failure location. SIF values are representative of the significance of the stress in each location, and also account for the consequences of having pores in these locations [20]. Similar concepts implementing SIF calculations have been proposed in fatigue life prediction approaches that examine the effects of pores on the fatigue life of an AM part [21]. The relationship between pores and fatigue life has also been explored through comparison of stress concentration calculations [22] and various crack growth equations [31, 32]. All these

14

studies have focused on the pores produced by a different AM method called laser powder bed fusion instead of DED. Using similar techniques in the future will produce acceptable prediction criteria for allowing repaired components to return to operation.

3 Materials and Methods

In this chapter, an explanation of all the processes used for this work are explained in detail. The coverage of these methods ranges from beginning to end for the work that was done on every single blade involved in the repair and testing process, as well as the work that was completed before and after to allow for smooth operation along the way.

3.1 Repair Process

The blades that were repaired for this project were retired after being used in the field for multiple years, with some of the blades accruing several thousand cycles of use. To begin the repair process, a portion of the blade was removed to simulate the removal of a damaged portion of the blade [1]. This was done by removing trapezoid-shaped sections from the blade on the trailing edge and the leading edge that were near, but not in, high stress locations, similar to the shapes shown in Figure 8. Once these sections were removed using wire electrical discharge machining (EDM), the blades were repaired using a DED process to fill in the removed sections. In this type of process, the laser moved parallel to the edge while Ti-6Al-4V metal alloy powder or wire was deposited into the path of the laser to create layers of deposited material that moved from the inside to the outer portion of the blade. The blade was stress relieved following the AM repair.
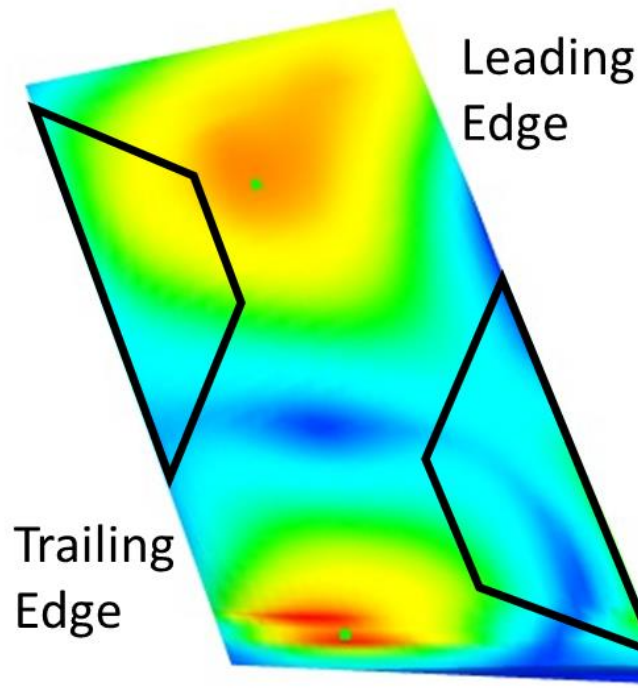
Figure 8: A maximum principal strain plot for mode two bending that shows the areas in which the repairs were made. The black trapezoid shapes outline the areas that were removed from the blades before the repair process began.

In total, 17 blades were repaired using the LBP-DED process, and 11 blades were repaired using the wire DED process. The blades came from three different rotors, identified here as A, B, and C. Rotors A and B were repaired as individual blades after being cut off the blisk, this applied to both types of DED repairs. Rotor C was repaired only using the LBP-DED process and done so while still attached to the blisk and it implemented a power table to modify the laser power that was developed after the repairs on rotors A and B were already completed. This power table was created by the LBP-DED developers to optimize the parameters being used to repair the blades by creating a dynamic program based off the thickness of the blade section. The goal was to decrease the power as the thickness of the blade decrease to prevent overheating the material. Once the repairs were completed, the blades from each rotor were polished back down to nominal geometry.

17

This was required due to the excess amount of material that was required during deposition to fill in as much space in the removed blade section as possible.

3.2 FEA Stress Analysis

A finite element analysis (FEA) model was created to approximate the stress that the blades would experience when being tested in vibration bending fatigue. The original blade model was obtained from the manufacturer for a representation of the blade before the repairs took place. After repair, the blades were scanned using a blue light 3D scanner called an ATOS scanner, which allowed for a new 3D model of the blade geometry to be created that implemented the changes from the repairing process. After combining the original geometry and the newly repaired geometry, the model was meshed in ANSYS to allow for mechanical simulations to take place. All these steps were completed before the blade model was received for further analysis completed by the author.

The configuration of the test was designed such that the blade was experiencing a mode two vibration frequency of approximately 3,000 Hz. To simulate the conditions of blade to mimic the broach block configuration. This broach block was used in the vibration testing set up as a way to clamp the blade and ensure there would be no movement during the testing procedure. Next, a modal analysis was created that targeted the second mode of bending in the blade. For simplicity purposes, the only mode of vibration that was selected for this analysis was mode two. This was completed to give the maximum principal strain map on the surface of the blade model, which can be seen in Figure 8. Later, these strain values were converted to stress and used in tandem with the measured stress from the testing process to create a more precise stress value at various locations on the blade.

This FEA process was also used to locate the areas in which the strain gages would be placed for testing purposes. These gages were intentionally applied to the areas of the blade that were expected to undergo the highest stresses during the second mode of bending. Precise placement of these strain gages resulted in more accurate recording of the maximum strain being measured at each step of the test.

3.3 CT Scanning

Computed tomography was used as a nondestructive evaluation process to analyze the internal defects that were created during the repair process. Computed Tomography (CT) scans combine thousands of X-rays into one stack of images to show a two-dimensional cross section at a specific point in the three-dimensional object that was scanned. Using the CT scanner software, these two-dimensional cross section images are compiled into one stack of CT images that can be opened in an image processing software as a stack of images that represent the overall three-dimensional volume. The processing software that was used to analyze these defects and take measurements is called ImageJ [23].

The act of conducting a CT scan is a multi-step process. It begins with confirming that the CT machine and computer are connected to power and turned on. Both machines need to be functioning properly to start a scan because the two directly communicate with one another. The CT scan will not start without controls that are only accessible from the computer that runs the CT scanner. After these connections have been confirmed, a homing process is started that will find the boundaries inside of the scanning chamber and record these boundaries as the limits of any movement that may occur during the scan process.

Since the CT machine uses X-rays to scan the components inside of the chamber, there is a short warm-up process that is required to ensure that the X-rays are communicating with the detector properly. This warm-up process is called auto-conditioning. It consists of a step process that slowly increases a target voltage that the scanner must reach before moving to the next voltage step, with the final goal being 225 kV. Once this goal is reached, the machine must hold this voltage value for 10 minutes to be considered ready for operation. A scan that is performed without this step will most likely fail due to software crashes when the scanner cannot hold the desired voltage throughout the scan.

Once the machine has been prepared for operation, the specimen can be placed into the chamber. The platform the component is placed on has the ability to fit multiple types of holders for different types of specimens, ranging from a flat plate that is meant for large parts, to a small clamp that is made for small specimens. For the scans in this study, a large clamp was used to ensure that the blades would not experience any shift in orientation during the scan. Any movement during the scan process would create problems in the reconstruction process of the scan. The dovetail of the blade was clamped to allow it to stand vertically, with the tip of the blade being the highest point while in the clamped position. Tightening the specimen securely was very important in order to keep the process as consistent as possible between scans. Once the blade was secure, the door to the scanning chamber was closed.

The CT machine is capable of two types of scans: circular and helical. A circular scan consists of a set magnification and specimen height, where there is no change in either parameter through the duration of the scan. This means the part only rotates during the scan

and there is no movement up or down. A helical scan is used when the desired magnification is too high to capture the entire area of the specimen in one window. To capture the entirety of the specimen, an upper and lower bound for the specimen height must be set. These bounds allow the specimen to move up and down within this range, while also rotating, to fully capture the area of the part that is too large for a circular scan. Due to the size of the blades in this work, the helical scan was used to capture the full airfoil region, ranging from the dovetail all the way past the tip. This was the equivalent of combining three circular scans that would cover the bottom, middle, and top of the blade. The downside to using a helical scan as opposed to a circular scan is that it takes longer to complete the scan, and it creates some image artifacts that make the image processing slightly more difficult. For this work, however, it was more important to cover the full volume of the blade and simply deal with the imperfections of the scan.

In the CT software, the helical scan selection was made to begin the set up process for each of the scans for the blades in this project. This opened a series of tabs in the software for various steps of setup parameters to be adjusted. The first tab was called position, where the height, voltage, current, and magnification of the scan are set. Validating the specimen was in the correct view of the scanning apparatus was most important when starting the position tab. At this point, the specimen was already clamped inside of the scanning chamber and the door had been closed. This allowed for the X-rays to be turned on that showed a live view of the blade inside of the machine. A panel of controlling joysticks was used to rotate, raise or lower, and adjust the magnification on the viewpoint of the blade. The height controls for the CT machine are working in the y-direction of the chamber space. It should be noted that for a CT scan such as this, the x-

direction stayed in a locked position as to prevent any changes in the centering of the object. The zoom adjustments that made changes to the magnification were done so by moving the blades in the z-direction of the chamber.

Since there were no controls available to move the specimens from left to right that would aid in the centering of the objects and the holder, slight adjustments to the gripping were required to accurately center the blades in the view of the scanning head. This was done by looking at the blade in the software viewing area with the x-rays on, then turning off the x-rays to open the door and move the blade in the grip accordingly. This process was repeated until the blade was properly centered in the viewing area of the software along the entire scanning height that was desired. At this point, the magnification of the scan was set using the zoom joystick from the control panel. The goal of the magnification adjustment in these scans was to get as close to the object as possible without losing any of the area of the specimen during the rotation that is required for the scan. Meeting this goal was done by leaving enough space on the edges of the blade from all angles that would allow proper capturing of the entire volume. If there was any point during the 360 degree rotation where a section of the specimen was blocked by the edges of the viewing area in the software, then the magnification was lowered to make sure this section would be fully captured in the images. The final magnification setting was given in µm, and this need to be documented as it was the voxel size for that given scan.

Once the centering and magnification adjustment was complete, the top and bottom of the blade was located and saved as the upper and lower bounds of the scan. The CT software required that these bounds be validated by using the y-direction joystick to move past the saved location and make sure there would be no interference with the other objects

inside of the scanning chamber. After these bounds were confirmed, the positioning tab setup continued with the calibration of the current and voltage of the scanning head. Calibrating these parameters is what allowed the CT scanner to penetrate through different types of materials and produce a similar outcome. It started with locating the thickest section of the area that was going to be scanned. Typically, this section was the base of the blade, looking from the trailing edge side to the leading edge side. While the x-rays were turned on, there were measurements for the intensity of the brightness that are being observed in the viewing window of the software. The goal was to have this brightness intensity read about 62,500 when looking at the thickest portion of the object to ensure that there would be no over-exposure to the images once the scan was completed. The over-exposure would cause the intensity of some pixels to max out on the brightness scale, thus causing a loss of detail in the images that were produced from the scan.

Adjusting the brightness intensity was done by increasing or decreasing the voltage and current in the CT scanner. The maximum voltage for this CT machine was 225 kV, but the typical range for these scans was between 190-200 kV. The typical range for the current was between 140-150 microamps. Increasing the voltage or current in the machine caused the brightness intensity to increase. These parameters were slightly adjusted to reach the brightness intensity goal of 62,500. The last thing to check in the position tab was the exposure and the gain. For these scans, the gain was maxed out at 24.0 dB, and the exposure was set to 500 ms. Confirming these parameters completed the setup for the position tab, allowing for advancement to the Reconstruction tab of the scanning process.

The second tab that required some input is the reconstruction tab. Here, the position of the object was captured from the front view and the side view as seen from the viewing

window of the software. Before entering this tab, it is best practice to have the front view of the object already selected. Once this was ready, there was a button in the reconstruction tab that said, "acquire images on which the volume of interest can be defined." Pushing this button took a snapshot of the specimen in the current position, as well as the position it was in after a 90 degree rotation inside the scanning chamber. These two views of the object were used to select the bounds of the scan. Red boxes appeared around each of the snapshots that could be changed by clicking on the edge and dragging towards or away from the blades to better capture the areas of interest. Editing this selection directly relates to what area of the blade was going to be scanned during the process. The goal was to capture the entire blade in both views to make sure there was no material being left out of the scan. This was the only parameter that needed to be changed from the default for the reconstruction tab.

The final tab was the acquire dataset parameters. The first option on this tab was to give the scan files a name. This name would be associated with the folders of the data that was produced, as well as each individual image that was created in the reconstruction process after the scan was completed. After the name was saved, there were values under the shading correction sub-category that were adjusted. The first was to change the frames to average value from 60 to 49. Next, the number of images value was changed from 1 to 4. Doing this created enough time per image to create a high quality scan. Below these options was the projection setup sub-category. Here, the box was checked to minimize ring artifacts during the scan. The value for the projections selection parameter was also changed from 720 to 1080. Finally, the frames per projection was changed from 1 to 4.

These parameters increased the total number of projections and created an estimate for how long the scan would take based on the size of the specimen and the time per projection.

In the acquisition sub-category, there was a button that contained two cog wheels overlapping. This was the safe position selection, and it was very important to the operation of the scan. Clicking this button caused another window to pop up in the software that gave options for setting a safe position. The safe position was the height at which the specimen was completely below the viewing window in the software, which also meant that it was a safe distance away from the scanning head to prevent any damage to any of the components in the scanning chamber. Setting this position involved first checking to see if the viewing window was in live mode by making sure the eyeball button in the top left was red. Then, the object was lowered using the y-position joystick until the viewing window of the software was completely empty. Inside of the safe position pop-up window was button that saved the current height as the safe position for the given scan. Pressing this button made a green check mark come up next to the button that meant the safe position had been saved successfully. Before exiting this window, it was important to check the brightness intensity level at the bottom right of the window. This value was required to be inputted into the white target parameter value in the shading correction sub-category so that the CT scanner would have a specific brightness intensity that the white pixels should be shown as. This brightness value being observed was meant to be very similar to the brightness intensity that was set in the position tab and was not supposed to be higher than 64,000. If either the value was greater than 64,000 or significantly different than the value that was set in the position tab, then the safe position window was closed, and the voltage or beam current was adjusted in the position tab to correct this issue. This was repeated until the two

intensity readings were similar. If the brightness intensity was close to the original set value, then the acquisition process continued.

After all these changes in the software were completed, the warmup timer in the acquisition sub-category was changed from 1 to 3 minutes and the correct reconstruction computer was selected for the data to be sent to. To start the scan, the acquire button at the very bottom of the screen was selected and the warm-up timer started. The warm-up of every scan consists of two parts. Once these two automatic steps were completed, the projections of the scan started and continued as the blade rotated and raised on height until all angles were captured from top to bottom. Completion of the scan was known when the software returned to the home screen where the type of scan was to be selected. This meant the data for the scan had been sent to the reconstruction computer and was ready for post-processing.

The software used for post processing the CT scan is called CT Pro 3D. In this software, various parameters can be adjusted in order to improve the visual quality of the scan. The final product is a stack of images that represents the specimen volume that was scanned in a two dimensional format. For this post-processing to take place, the files created from the scan were located. Inside of this folder was a CT Pro 3D file with the same name as the one given when the scan was started. Opening this file also opened the CT Pro 3D software on the first tab, which is called image. The only important step inside of the image tab was to observe the pictures of the specimen on the right hand side of the software window. Here, there were two projections showing the same angle of the object during the scan that were taken at the beginning and the end of the process. These images were used to confirm that there was no movement in the scanning process. If there were significant

differences between the images, there was a high chance that the scan would need to be restarted. Little to no difference between the images meant the post-processing could proceed.

The next tab in the CT Pro 3D software was called center of rotation. Here, the most important change was mask radius percentage. This feature was found on the left side of the software window when scrolling down about halfway through the page. The default was set to 100%, and this was lowered down to 97% to comply with a recommendation that was given by the manufacturer. After changing this value, the page was scrolled down to the bottom where the accuracy was changed to high quality and the center of rotation option was set to automatic. Completing these steps meant the center of rotation validation could begin by clicking start at the very bottom of the screen. This process outputs two pixel values that should be nearly identical, each of which represents a parametric that is calculated using the center of rotation of the projections that were captured during the scan. If these two values differed by larger than two pixels, then the scan was re-done. Confirming these pixel values to be within two meant the process could continue.

Setup was the next tab in the CT Pro 3D software. This section allowed for some significant changes to be made to the way the images looked after being post-processed. The most significant change for each of the scans that were completed was to adjust the level of beam hardening in this tab. To compare the different levels of beam hardening, the check box under the sub-section of beam hardening was selected and the start button was pressed at the bottom of the page. Activating this selecting caused the software to produce an example of every level of beam hardening for the given area of the scan, thus allowing a selection to be made for the one that looked the best for analysis. A metric that was used

to decide which beam hardening was the best involved measure the contrast of the edges of the blade versus the background of the image. Finding a good contrast between these two areas of the image meant that the processing for analysis could be completed much more easily. To do this measurement, a red line was drawn across the section of the blade in the viewing portion of the software. The line was drawn by left-clicking on the left side and then clicking again on the right side of the blade to create a line that span across the middle section being displayed. In doing this, a graph appeared on the left that represented the level of brightness intensity along the line, indicating where the two edges of the blade section were located along the line. These edges on the graph were meant to be sharp and tall, which meant the contrast between the object and the background was sufficient for analysis. The typical value for beam hardening in this work was a level of either three or four.

The final tab in the CT Pro 3D software was volume. Here, the full area of interest for the object was selected and exported. To capture the area, the edges of the red boxes around the images were adjusted until all areas of interest were included in the box. Then, the page was scrolled down to the bottom where the export style was chosen. For every scan in this project, a single tiff stack was chosen. This produced the number of images required to completely capture the entire scan area. These images were compiled into a folder that numbered and sorted them from the bottom of the object to the top. This stack of tiff images is what would later be used to complete all image processing for analysis and measurements of any visible defects in the repairs.

3.4 Image Processing using ImageJ

When a CT scan is conducted, an important part of analyzing the results is knowing what the voxel size is for that scan. Voxel size, also known as volume pixel, is the measurement of the three-dimensional pixel and it represents the length of each side of the cube that is seen as one volumetric pixel. In this case, the voxel size was about 28 µm. Therefore, the height and width of the volume pixel was 28 µm, as well as the distance between images being shown in the CT stack. It is important to know what the voxel size is for both measurements and analysis, but also because accurate defect measurements in CT scans are best obtained from defects that are typically three times the voxel size or larger. Having a voxel size of 28 µm means defects were accurately measured at a minimum size of around 85 µm.

All CT images that were captured in this project were put through a series of processing steps to measure and analyze the results of the repairs for the turbine engine blades. The software that was used in order to complete all of this image processing is called ImageJ, or Fiji. This software has many features that improve the ability to measure all sorts of images taken for various purposes. The first step in processing any set of images with this software was to import the images. This was done by dragging the folder in which the images are contained and dropping it into the ImageJ window. A pop-up window appeared that is shown in Figure 9, named import image sequence, with a selection to change which image was started on, how many images to import, and what the scaling of the images should be. When first importing a CT scan, it was almost always the full stack starting from the first image to get the best idea of what the scan consisted of. There were also options at the bottom of this window to sort the names of the images numerically, open

as a hyper stack, and open as separate images. The scans were always sorted numerically

due to the order of the images being crucial to the processing steps. A virtual stack is helpful

because it opens much faster, but it is limited in terms of the processing steps that can be

completed, so this was typically avoided. Opening as separate images for this project had

no benefits whatsoever. The OK button at the bottom of the window was selected once the

desired selections were made.
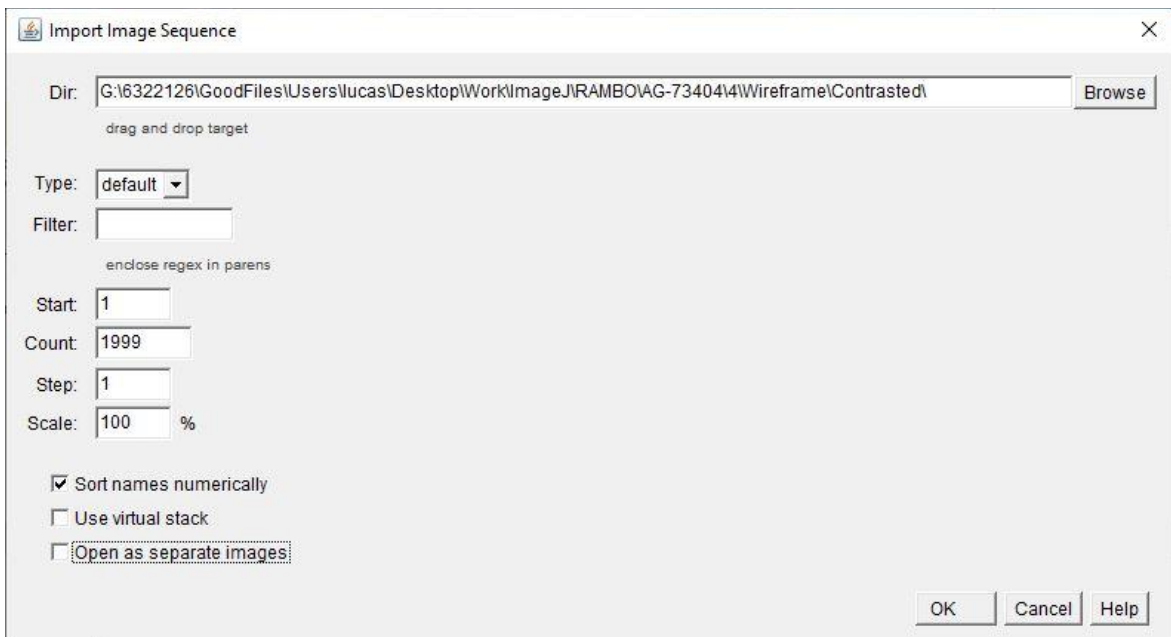
Figure 9: Import Image Sequence pop-up window in ImageJ

After the images were done importing into the software, the first step was to adjust

the contrast to make the pores more obvious more analysis. Contrast options can be opened

by selecting image ion the tool bar of ImageJ, then adjust, and brightness/contrast. The

pop-up window for this selection is shown in Figure 10. The goal with this adjustment was

to raise and lower the minimum and maximum detectable pixel intensity in the images so

that the defects stand out from the rest of the blade volume. Once this was achieved, the

apply button was selected to save these changes. Typically, there were no changes in the brightness for the work done in this project.
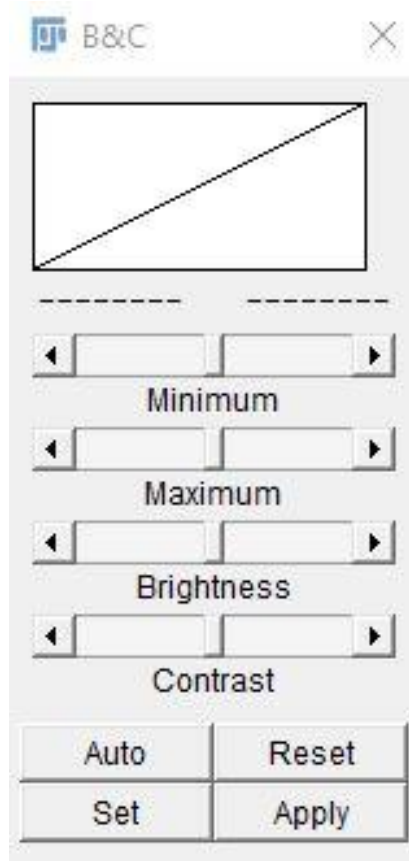
Figure 10: Brightness and Contrast adjustment pop-up window from ImageJ

After adjusting the contrast of the images, a tool was used to isolate the defects from the rest of the blade in the images. This feature was found by selecting process in the tool bar, then subtract background. This caused the subtract background pop-up window to appear, shown in Figure 11, with options on how to change the subtract background process. In this work, the light background and preview options were always selected. Light background caused the pores to appear black and the blade volume to appear white. The preview function simply allowed a view of what the current selections were going to change on the images, so this was helpful in deciding what to use for the process. The

31

rolling ball radius is essentially what size of defects will be left once the process is complete. Anything larger than this size was included as a dark spot in the resulting images that would eventually be counted as s defect. The typical size for this process that was selected for the rolling ball radius was five pixels. The OK button was selected once the correct parameters were chosen.
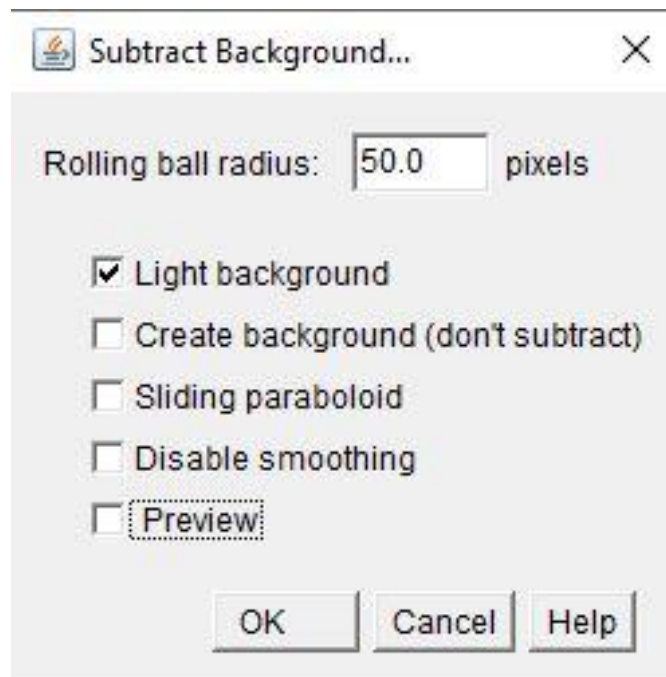
Figure 11: Subtract Background pop-up window from ImageJ

The next step in the image processing approach was to set a threshold to capture the pores in the newly modified images. The subtract background tool left a stack of images that were mostly white with the defects being represented by black clusters of pixels. The threshold feature is meant to capture those black pixels in order to convert the image to binary, meaning a pixel is either completely black or white. To access the threshold adjustment window, image was selected in the tool bar, followed by adjust, then threshold. The tricky part about this step was to try to adjust the threshold so that only the pores were

being selected and not any other noise that tends to occur when CT scanning an object such as these blades. Once the most ideal threshold value was found, the images were converted to binary by selecting process from the tool bar, then binary, then make binary, This opens the convert stack to binary window. Every option on here was kept as the default for this project, and the OK button was selected to confirm the selections.

To complete this process, the pores were measured in the repair area of the blades. Now that the images were binary with all background pixels being solid black and all the pores being solid white, it was very simple to measure the pores. Analyze was selected from the tool bar, then set measurements to choose what will be measured in the process. After these selections were made, then analyze particles was selected from the same menu, opening the pop-up window shown in Figure 12. Here, the results and summary were of interest, and all pore sizes and shapes were measured. The process was started after these selections were made that would output a spreadsheet of all the items being measured that was called the results. Displayed on this window were many different measurements and calculations from every image included in the stack of the CT scan. The most important column for this analysis was the feret diameter measurement, as this was the best way to measure the pores in the repair scans. This results window was saved as an excel spreadsheet for further analysis.
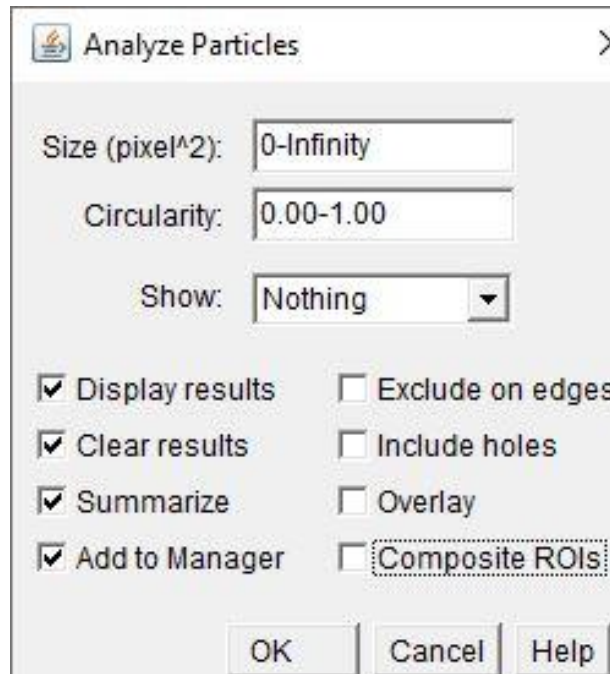
The final step for image processing using ImageJ was to complete a 3D measurement of the pores in the CT scan. Measuring the pores in 3D was completed using the 3D object counter feature in the software. First, the types of measurement that were going to be made had to be selected, like the first set of measurements from above. Selections were made by choosing analyze in the tool bar, then 3D OC options, and choosing which things should be measured in the process. The measurement feature was found in the analyze section of the tool bar, then selecting 3D object counter. This selection opened the 3D Object Counter pop-up window shown in Figure 13. Completing this measurement also produced a window with results that could be saved as an excel file, with all the measurements including the z-direction of the stack. This means the measurements spanned across multiple images at a time, not restricted to just one slice from the stack of the CT scan. Doing this allows for some interesting calculations to be done with the

previously explained two-dimensional measurements that were obtained from the analyze particle measurements.
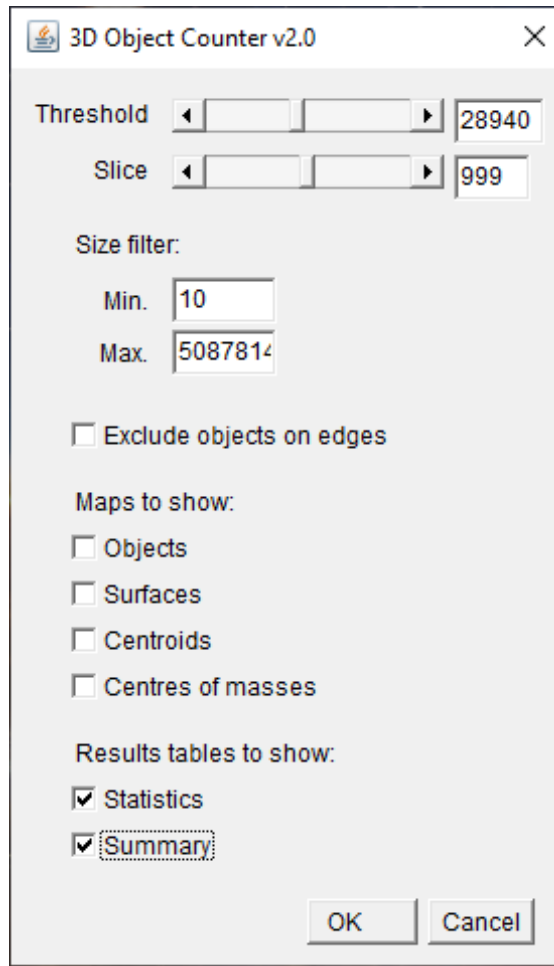
3.5 Image Processing outside of ImageJ

The biggest issue with using the analyze particles feature to complete two-dimensional measurements is that it measures every feature on every image and counts it as an independent pore. The three-dimensional measurements do fix this issue, as these results include the images before and after the pores for each individual slice, allowing for a volume measurement across images to be calculated. Using each of these independently

35

provides helpful insight to the results of the repair, but the real advantage comes when using them together. Since the three-dimensional does not give information on the diameter of the pores, and the two-dimensional measurements do not consider the full volume of the pores, combining them allows for the full picture to be seen. The combination of the two methods was mainly used to see what the largest diameter for each pore was in order for it to be sorted and filtered for further processing.

For the two-dimensional analyze particles tool, the results were output as an excel file that gave information for the feret diameter, the x location, the y location, and the slice number that each of the measurements took place on. The 3D object counter results gave the volume, centroid location in x, y, and z coordinates, and the dimensions and location of a bunding box that went one pixel outside of the furthest point of every pores in all directions. To complete the merge of these two methods, an excel file was created to group all the results from the 2D measurements into the bounding boxes from the 3D measurements. The bounding boxes encapsulated all of the pixels that could belong to a single pore, meaning that matching up the boxes to the analyze particles results would create a set of results that concisely combines the two methods. Combining these measurement techniques provided a set of data that included both the diameter of the pore and the full volume that it filled, allowing for the most precise analysis to be completed.

After these groupings were made, the data was now able to be viewed in the most useful form. Since each of the 3D measurements were focused on volume, using the two techniques together made it possible to see the single largest feret diameter measurement that was found in each individual bounding box. Pulling these values into one dataset then created a list of all the defects being measured in the entire repair, along with the absolute

largest diameter that was measured for each of those pores. From this list, important data could be obtained for comparison amongst repairs that included: total number of pores, max pore size, number of pores over a given value of diameter size, and number of pores under a given value of diameter size. All these values were compiled into a table that was used to analyze the effectiveness of each repair type on the different rotors that were tested in this project.

3.6 Vibration Bending Testing

The method used for testing a jet engine blade in application relevant loading was to attach it to a hydraulic shaker and vibrate it at the mode two resonant frequency to create a large strain, and thus, a large stress that caused failure. To do this, the blade was inserted into a custom broach block, shown in Figure 14, that was tightened to 120 foot-pounds. The broach block was then bolted down onto the top of the Unholtz-Dickie Electrodynamic Shaker System, as shown in Figure 15. Properly securing this apparatus was very important because any movement of the blade in the broach block system could have resulted in inaccurate test results. The sensitive nature of the vibration fatigue testing requires a high level of precision and minimizing the unnecessary movement of the specimen is a large part of keeping the test accurate. This method has been used in application relevant loading for previous work with similar configurations [34, 35].
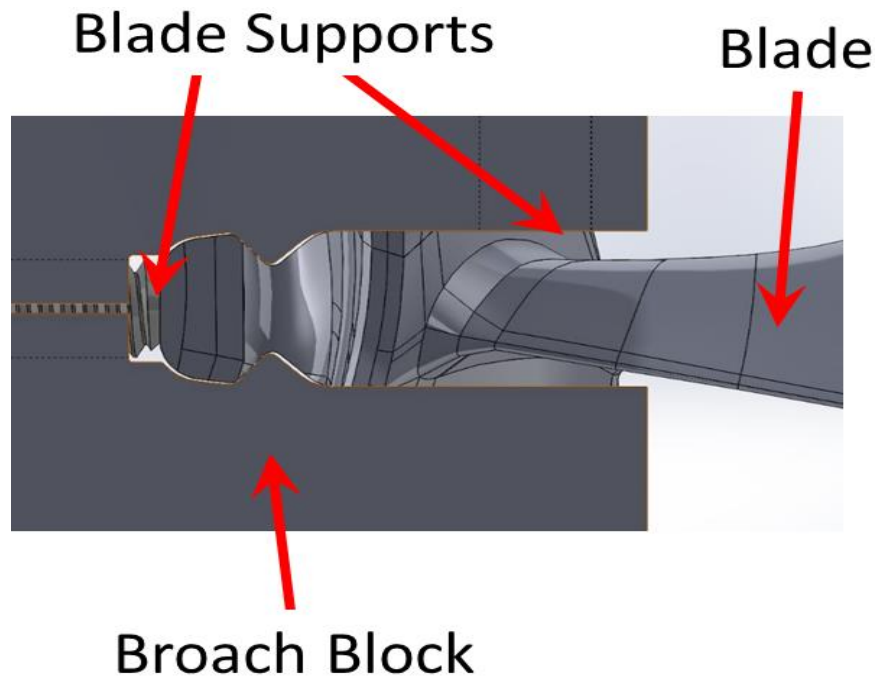
Figure 14: Broach block set up used for testing the fatigue life of the repaired blades
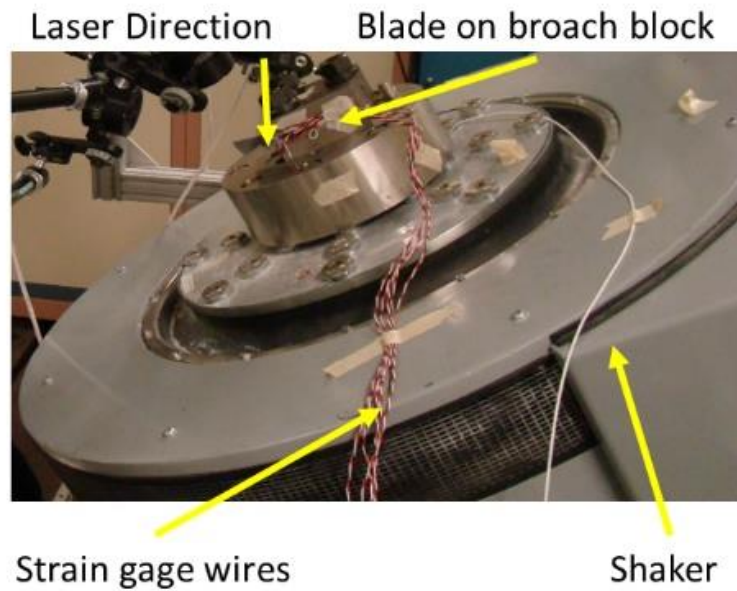
Figure 15: Testing Apparatus set up of broach block and blade on the Hydraulic Shaker

Uniaxial strain gages were attached to the surface of the blade with a strong bonding adhesive. The gages were strategically placed ion the max principal strain direction. These

gages have attached wires that fed into a signal conditioner that was used to calibrate the strain output. The signal conditioner was used to correlate the output signal of the strain gages to one microstrain per millivolt. This unit calibration was done by following a discrete list of steps provided by the conditioner manufacturer until the desired voltage value was reached. A Polytech PSV-500 Scanning Laser vibrometer was pointed at the tip of the blade closest to the trailing edge corner to measure the velocity during testing. To prevent any issues during the test, the shaker was tilted 45 degrees so the laser could be pointed perpendicularly to the surface of the blade. Creating this angle was important for velocity measurements because the vibration caused during the test is vertical with respect to the shaker position. Therefore, the blade being at a 45 degree angle allowed for the laser to also be at a perpendicular 45 degree angle and give the most accurate velocity readings. The strain and laser signals were then transferred to the acquisition computer to measure the strain at various frequencies as well as levels of velocity and displacement.

Output signals for the strain and velocity fed into the computer software that was used to control the shaker testing and record the data being observed. These strain and velocity measurements were used to create a proportional relationship for the blade by plotting the points and using the equation of the trendline that represented the relationship of the data points. Using the strain-to-velocity relationship, velocity values were calculated with strains that ranged from 500 to 6,000 microstrain in increments of 300. The linear relationship was created, and test is controlled by these velocity values since the strain gages typically failed after about 1,000 microstrain due to weak adhesives being used to secure the gages onto the surface of the blade. These control velocities were then added to

39

the test schedule to give an accurate representation of the strain being experienced by the blade at each step.

To begin the testing process, sweeps on the blades were completed that went from high frequency to low frequency, with the goal of finding the resonant frequency for mode two within that range. These sweeps are run at a low acceleration value to prevent delamination of the strain gage from the surface and to allow for variation in the frequency and velocity, but to also prevent any large damage accumulation before the test is officially started. The peak of the velocity versus frequency graph gives a maximum velocity and associated strain for that sweep, even at the low value of acceleration. Multiple sweeps were completed at increasing acceleration values to complete the strain versus velocity plot that was then used to create the linear relationship using the trendline equation. Once enough data was collected to verify that the strain to velocity relationship is valid, the test was started.

Each step in a test consisted of the same number of cycles at increasing values of strain, which involved dwelling at sinusoidal amplitudes that creating the strain being measured. Since these steps were created by tracking to a value of velocity being measured by the laser, a warm-up process was required. This warm-up allowed the shaker to safely increase the strain in the part in a way that gave the shaker time to stabilize before increasing the velocity of the vibrations. Slowly moving up in velocity was a good way to make sure that the rest of the testing set up was working properly as well. Completing the warm-up meant the first step of the test was started, which was pre-determined based on an estimation of when the blade was going to fail according to previously recorded data. Once one step was completed, the next step began with a slightly higher strain. This process

continued until failure was expected in the blade, which was determined by a shift in resonant frequency from the original value [36-39]. In some case, restarting the test was required to compare the resonant frequencies from each run to validate failure or further drive the crack that has been formed.

When the test had stopped due to potential failure, the blade was removed from the apparatus and inspected via fluorescent penetrant inspection (FPI) for any cracks that were created during the testing process. If the test had stopped, and it was not due to a crack, then the test was restarted. The step that it had stopped on is finished by subtracting the cycles that had previously been completed to accurately determine how many cycles the blade had experienced at each level of strain. In some cases, when a crack was expected but not completely obvious, the blade was vibrated at the resonant frequency at large values of acceleration to grow the crack so that it could be more easily visible during the FPI post-test inspection. The failure stress was then calculated using Equation 1, which is an interpolation of the strain from the both the step before failure and the step that caused failure, along with the elastic constants for the material, E=110.3 GPa [40, 41]. This gave stress that caused failure based on the strain that was being experienced by the blade and the stress versus number of cycles to failure plot is created. The overall procedure has been completed for aluminum, nickel, and titanium based alloys with validation against constant sinusoidal dwell results [42-44].

$$\sigma_a = \sigma_{pr} + \frac{N_{fail}}{N_{step}}\left(\sigma_{fail} - \sigma_{pr}\right) \tag{1}$$

3.7 Typical Failure Location

Using the FEA strain locations and the preliminary baseline testing, a typical failure location was found. All of the non-repaired blades that were fatigue tested on the shaker set up failed at the root, shown by the number one displayed on Figure 16. This is the highest strain, and therefore the highest stress, that the blades experienced on the shaker when vibrating in the mode two bending shape. The other three regions are also area of high strain but given as a percentage of the maximum from area one. Location three is the second highest strain on the blade at 98.2% of the maximum value. The fourth location is next with 94.4% of the strain at location one, and the least of these locations being 76.9% of the maximum strain at location two. Making the cuts and repairs near, but not in, the two highest strain locations was the goal to push the limits of the repair processes and find out what the limitations really were. This also allowed for larger pores to be created without causing a huge drop in mechanical performance due to the location of the pores not being in the highest strain area of the blade.
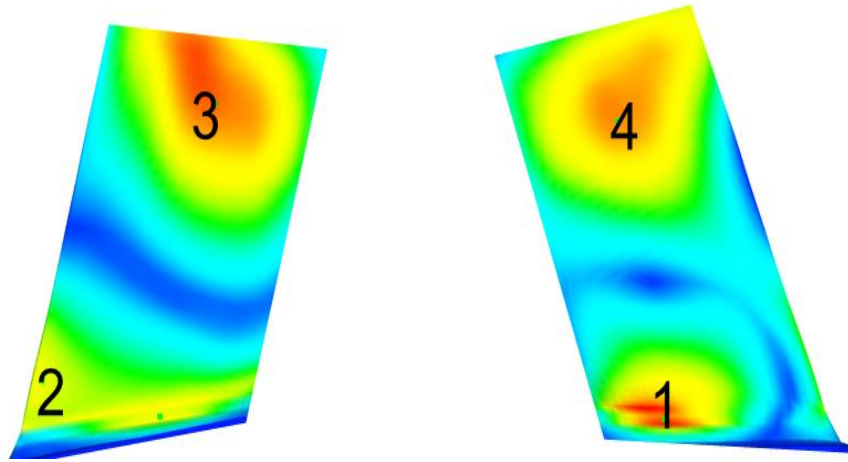
Figure 16: Maximum principal strain plot from FEA of a blade in mode 2 bending that highlight the top four area of highest strain

4 Wire DED Results

In this chapter, the wire directed energy deposition repair process is discussed. After the repairs were completed, the blades went through CT scanning, fatigue testing, and post-failure analysis. The results from vibration fatigue testing and CT pore analysis are provided to allow for direct comparison to the LBP-DED process results. Any additional data that was used to create conclusions and comparisons is also provided in this chapter.

4.1 Repair Process

There was a total of eleven blades that were repaired using the Wire DED process. These repairs began once the correct section had been removed from each blade. All wire DED repairs were completed on blades that had been removed from the IBR. Figure 17 shows a general diagram of how the material was added to the blades during this process. The blade was secured in place beneath the deposition head in the proper area needed for the Ti-6Al-4V wire feed to reach the surface. This wire feed was heated to allow for easier melting and deposition onto the blade. Once the wire contacted the blade surface, the 6 kW laser melted it into the gap of the blade in layers that started on the interior of the blade and moved out to the edge. The heat required to complete this process could not be contained solely to the repair area. This created a heat affected zone (HAZ) around the repair and in the base material of the blade. This boundary and heat affected zone is known for creating large defects because this is where the deposition must "turn around" and move along the repair in the opposite direction. Since the deposition could not be exactly precise on

matching the thickness and geometry of the blade being repaired, the deposited area was

thicker than the blade, as shown in Figure 18.
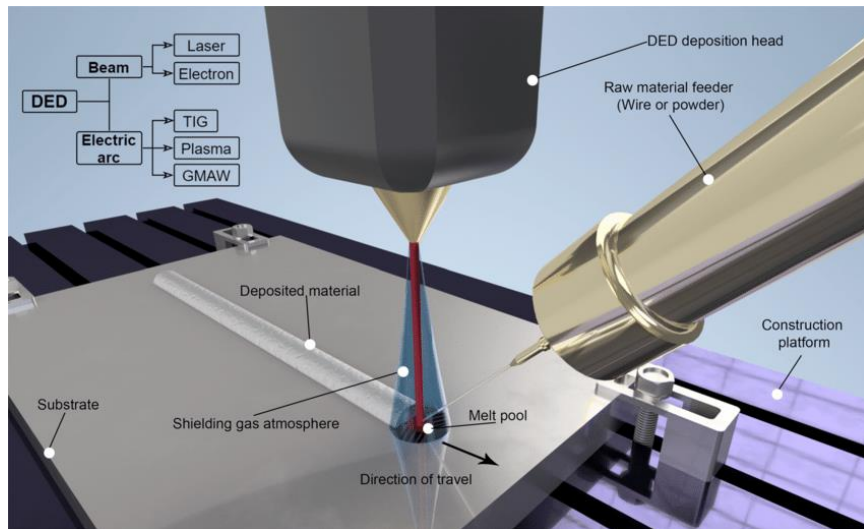
Figure 17: General procedure diagram for the wire DED process [24]

Figure 18: Final result of a wire DED process repair deposit before it was polished back to nominal geometry

4.2 Pore Size Distributions

Using the images created from conducting CT scans on the repaired blades, measurements were taken of the pores that were created during the wire DED process. As mentioned previously, these measurements were compiled into multiple data sets. A few of these datasets are shown below. Table 1 gives an overview of the measurements that were taken in the repairs. Here, the largest single pore diameter from each repair is given, along with the total number of pores, and the percentage of these pores that are larger than three threshold sizes: 100, 131, and 227 µm. These threshold values represent the sizes of pores that are rated as acceptable, not ideal, and unacceptable, respectively, in terms of what can be produced in a blade repair in order for it to continue functioning without failure. The important thing to note is that a significant number of pores being larger than the 131 and 227 µm values is concerning for a blade repair. Nearly half of all the pores in each repair are larger than the 131 µm threshold, and every single repair has several pores above the 227 µm mark as well. It should be noted that the total number of pores seems a bit low. This is due to the CT image processing eliminating many of the insignificant small pores that could not be separated from noise that is produced during the CT scan. However, all of the larger and more important pores were picked up in the measuring process and are the bulk of the focus for these repairs.

Blade #	Repair Location	Largest Pore Diameter (µm)	# of Pores	% > 227	% > 131	% > 100
A-1	TE	631	43	55.8%	79.1%	83.7%
A-4	LE	427	44	18.2%	45.5%	81.8%
A-5	LE	1322	32	37.5%	71.9%	100.0%
A-11	LE	1089	30	26.7%	63.3%	96.7%
A-15	TE	707	15	53.3%	73.3%	100.0%
A-18	TE	431	12	75.0%	100.0%	100.0%
B-2	TE	921	25	20.0%	52.0%	100.0%
B-5	TE	853	50	32.0%	74.0%	100.0%
B-6	LE	790	39	17.9%	48.7%	94.9%
B-10	LE	393	18	27.8%	61.1%	100.0%
B-20	TE	2183	62	41.9%	66.1%	95.2%

Table 1: CT pore measurement results from the wire DED repairs

Figure 19 shows the probability distribution function (PDF) of the pore sizes among all the wire DED repairs, blue being repairs from rotor A and red being rotor B repairs. This graph represents the probability of a pore being created versus the size that pore could be, given in µm. The area under the curve for each of the repairs represents the total probability of a pore being created up to a specific size. The peak of the curve represents the most probable pore size for each repair. A sharper peak at a lower value of pore size is better since this indicates an overall smaller range of pore sizes being found in that repair. Although peak at a lower value is more ideal, it is important to remember that there is still a 50% chance of a pore being created that is larger than this peak value. Using this type of graph, it is easy to see the inconsistency of the wire DED process. Both the probability and the pore size start at zero on the graph, but the curves continue to span a pore size of over 700 µm. The span of the curve is representative of the range of sizes that was measured in each of the repairs. The larger the span of the curve along the x-axis, the larger the pores were for that given repair. The maximum size along the x-axis of this graph was cut off at

700 µm to focus on the peaks of the curves in the smaller size ranges, but these curves do continue onwards past the end of the graph shown here.
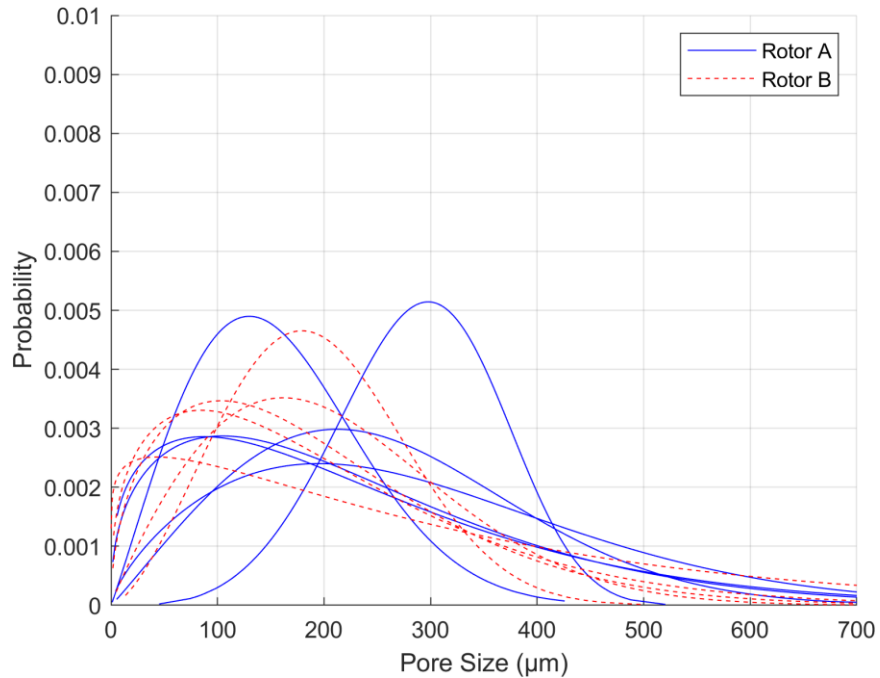
Figure 19: Probability density function for pore diameters of each wire DED repair from Rotors A and B

The next graph that was used to show the consistency of the repairs is the cumulative distribution function (CDF), shown in Figure 20. This graph shows curves that give the probability of a pore being created that are equal to or less than the size given by the x-axis. For example, going up from the 200 µm size will intersect the curve at a given value on the y-axis. This is representative of the probability that a pore will be created in that repair process that is 200 µm or less. The top of the curve approaches a value of one close to the maximum pore size found in each repair, confirming that the probability of a pore being created that is less than or equal to the maximum size is 100%. Like in Figure 19 that shows the PDF, some of the CDF curves continue off the chart past the 700 µm size. This is due to the maximum pore size for some of the blades being larger than this

size. Consistency is shown in a CDF when the curves end around the same pore size. This is not the case for the wire DED as many of the curves span a much larger range than the ones that are shown here.
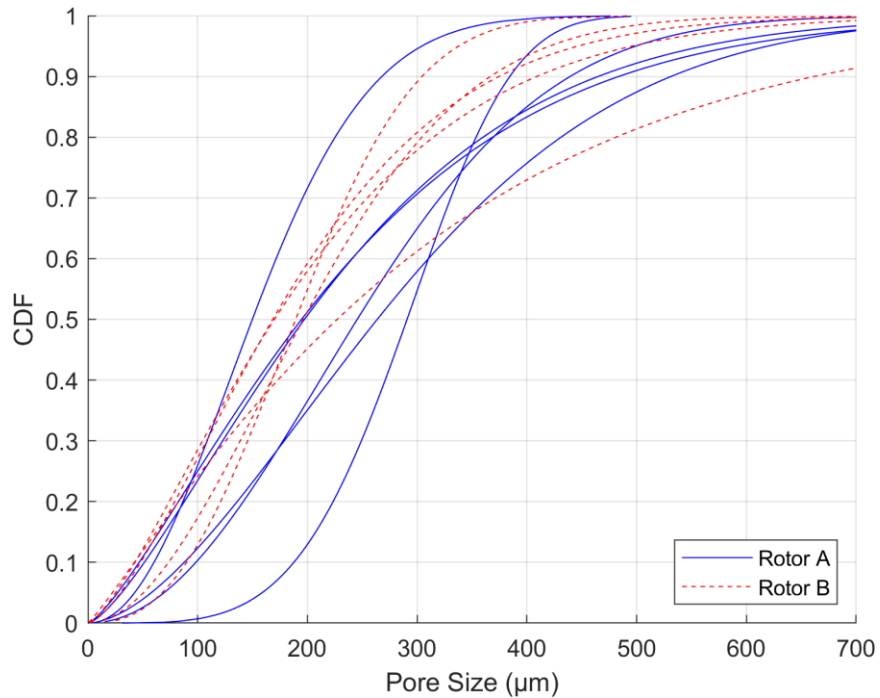
Figure 20: Cumulative Distribution Function for pore diameters of each wire DED repair from Rotors A and B

As mentioned previously, there is a maximum allowable pore size that was determined to be 227 µm. Pores over this size start to risk failure if there is formation near high stress locations. Figure 21 shows the mean diameter with error bars that give the range of standard deviation, as well as the maximum pore size from each repair in the wire DED process. When looking at these sets of data, it is apparent that the maximum pore from each repair is over the 227 µm allowable threshold that cannot be exceeded. In addition to this, the mean of six out of eleven wire DED repairs were also over 227 µm with every range of standard deviation also exceeded this value. There also seems to be no significant correlation between the mean or maximum pore sizes found in the repairs and the location

49

of the repair. Overall, the pores found in the CT scans for the wire DED repairs turned out

to be larger than the allowable size that was decided at the beginning of the project.
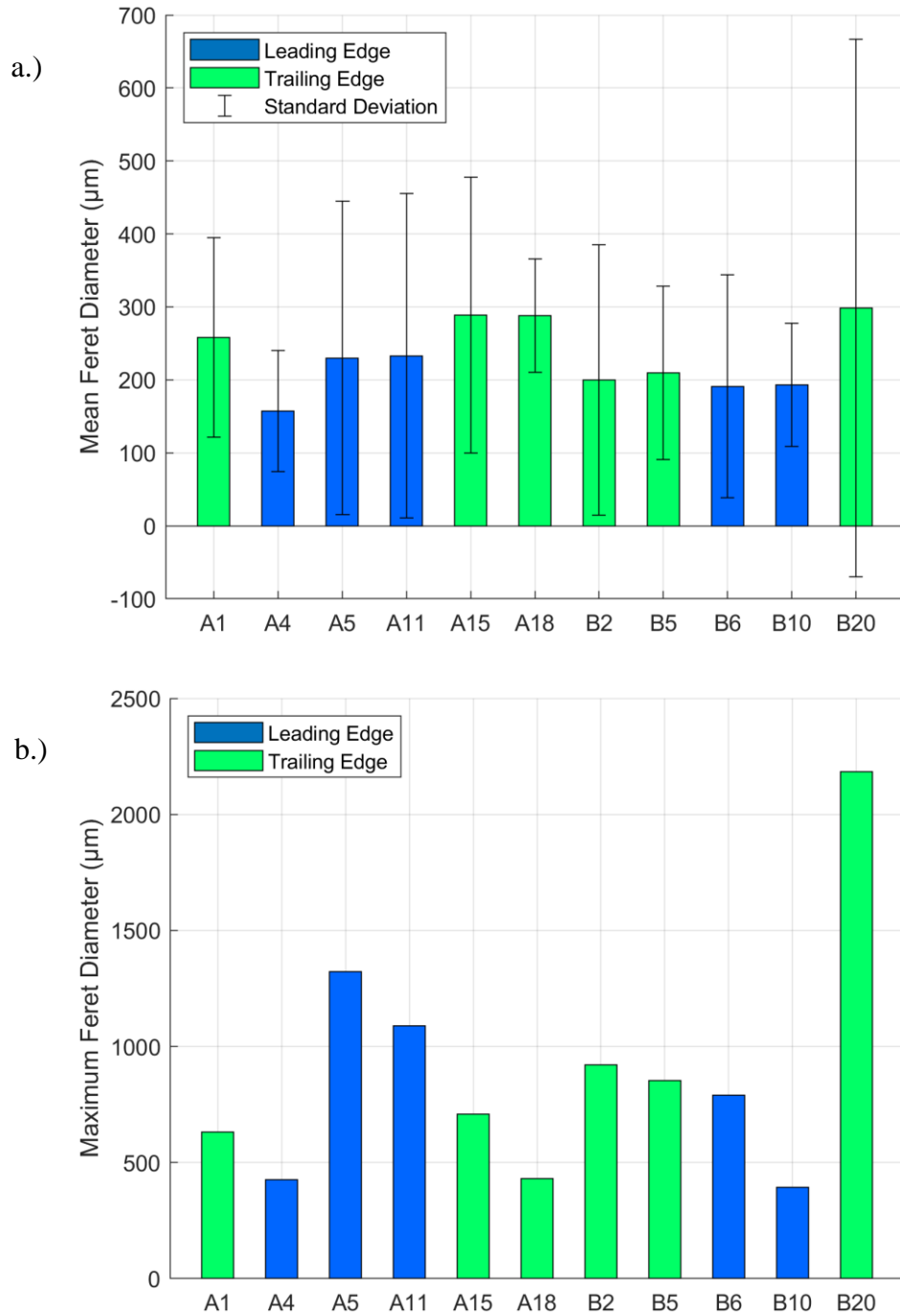
Figure 21: a.) Mean value of the pore size across each individual wire DED repair from Rotors A and B with error bars representing the standard deviation of pore sizes for each repair, and b.) max feret diameter found for a single pore in each repair

4.3 Fatigue Testing Results

Conducting vibrational fatigue tesing on the blades produced results for the failure strain and number of cycles to failure. The strain was converted into stress and used to create Figure 22, which is a stress versus number of cycles to failure. The stress value that was used here was determined by taking the strain from the strain gage that was placed at the root of the blade, then converting that strain to stress using the young's modulus. This means the failure stress that was used for every blade in this graph is the stress from the root of the blade, not the stress at the location of the crack formation. As shown in the plot, all but one of the wire DED repairs failed in the deposited material, away from the typical base material failure location at the root. Failures inside the repair material are marked on the plot with a plus sign over the orginal marker. The hollow markers represent the baseline blade testing data, with the blue diamonds showing rotor A nd the green squares showing rotor B results. The filled in versions of these markers give the results for the repaired blades that were fatigue tested. The solid black lines on the plot give 99% prediction bounds that were generated using the baseline data of the non-repaired blades.
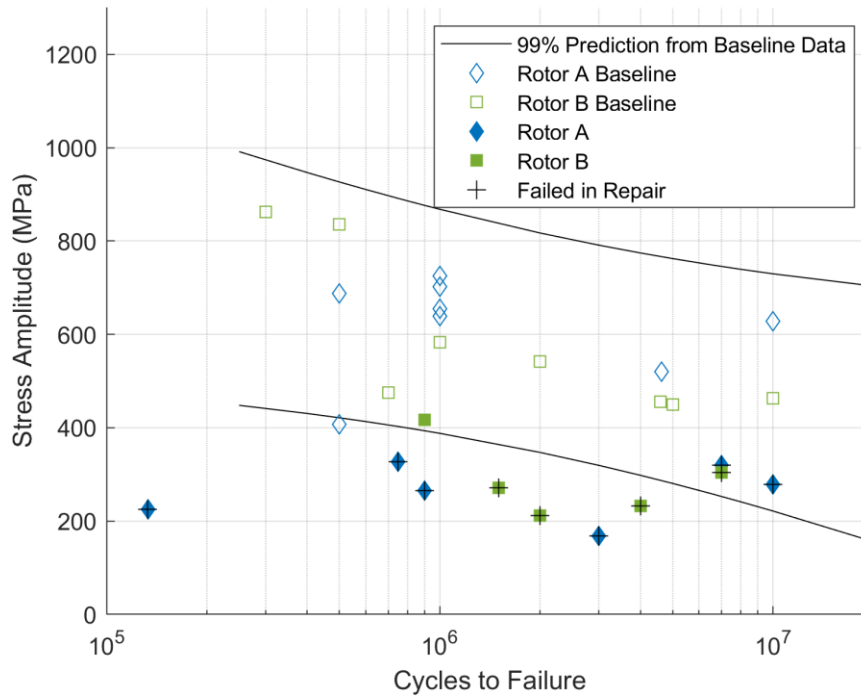
Figure 22: Stress versus Number of Cycles to Failure from vibration fatigue testing for each individual wire DED repair in Rotors A and B

Due to the type of step test that is conducted in the vibration fatigue testing procedure, there is a specific number of cycles required per step of the test. However, these steps do not begin immediately. There is a number of preliminary steps that are required to get the shaker up to the required speed for the first step to run smoothly. One of the wire DED repairs did not make it to this first step due to an incorrect estimation of the failure strain. This data point is shown on the far left near the bottom of the plot, very much outside the range of the 99% prediction data. Along with this data point, there are six other blades that failed outisde of the prediction interval. This is simply because the failure stress was too low for the given number of cycles to failure to be inside of the range. Ideally, the repaired blades would fall into this prediction interval to prove that the repairs were a successful alternative to normal baselined data. With only four of the wire DED repairs

52

being inside of this prediction area, and three of those four failing in the deposited material, these blade repairs would be classified as unsuccessful.

The full details of the failures from the wire DED repairs can be seen in Table 2. This table outlines the location of the crack that formed during fatigue testing, the number of cycles per step during the test, the failure strain that was measured during the test, and the failure stress that was calculated using the strain measurement. This table presents all of the important data in a way that is easily comparable among the different blades. The only significant correlation that can be made from this table is that all the leading edge repairs cracked on the edge and grew inwards, whereas the trailing edge repairs cracked more in the center of the blade. The cause of this correlation is presumably due to the location of high stress relative to the repair areas. The trailing edge repairs had a high stress in the mode two of bending that was very near the inner most portion of the repair. Conversely, the high stress near the leading edge repairs was a bit further from the repair line, making the edge more susceptible since this is where the defects were forming.

Blade #	Repair Location	Failure Location	Cycles per Step of Test	Failure Strain (µɛ)	Failure Stress (MPa)
A-1	TE	Middle, in repair	7.50E+05	2,522	327.64
A-4	LE	On LE, in repair	1.33E+05	1,730	224.65
A-5	LE	On LE, in repair	3.00E+06	1,213	167.90
A-11	LE	On LE, in repair	9.00E+05	1,952	264.72
A-15	TE	Middle, in repair	1.00E+07	2,136	279.10
A-18	TE	Middle, in repair	7.00E+06	2,415	319.92
B-2	TE	Root, in base material	9.00E+05	3,064	416.38
B-5	TE	Middle, in repair	4.00E+06	1,805	232.07
B-6	LE	On LE, in repair	7.00E+06	2,431	304.51
B-10	LE	On LE, in repair	1.50E+06	2,177	271.80
B-20	TE	Middle, in repair	2.00E+06	1,640	211.61

Table 2: Fatigue testing results for each wire DED repaired blade

4.4 Fracture Surfaces

After the testing was completed on each of the blades, the crack was fully propagated, and the blades were separated to expose the fracture surface. These fracture surfaces are shown below as Figure 23. Analyzing these fracture surfaces helps to give more insight into the reason that these failures occur. The images shown in Figure 23 are similar to all the fracture surfaces that were analyzed from all the wire DED repairs. The first fracture surface here is blade B-2 which is the only wire DED blade that failed in the typical failure locations and in the base material. This fracture surface shows striations that point towards a crack initiating at the surface along the bottom of the image. The next image is the fracture surface from blade A-5. On the right side of the image is a large lack of fusion defect that caused the initiation of failure for this blade. This was the largest pore found in the entire repair as it spans the full thickness of the blade, from suction side to pressure side. The final fracture surface of Figure 23 is from blade A-11. Similar to blade A-5, there is a lack of fusion pore across the thickness of the blade closer to the leading edge. This was most likely the cause of fracture initiation as well, which can be confirmed by the small number of striations that are pointing towards this region throughout the rest of the image.

a.)
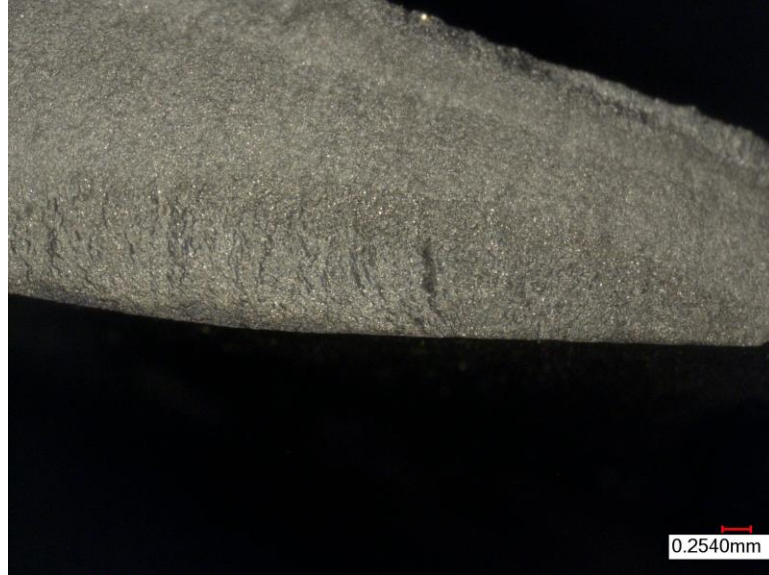
b.)

c.)

Figure 23: Fracture surfaces from wire DED repairs in blades a.) B-2 b.) A-5 and c.) A-11

4.5 Conclusions

The wire DED repair process results were quantified based on fatigue testing on a vibration shaker apparatus and CT pore measurements. A total of eleven repairs were completed on individual blades from rotors A and B. The goal to keep pores under a value of 227 µm in the repair area was not met due to large lack of fusion pores that were found in nearly every repair, regardless of the repair location on the blade. This was evident in the pore distribution analysis from CT scan measurements, as well as the fracture surfaces that were captured using an optical microscope that displayed the LOF pores causing crack initiation in the deposited material. One successful repair was found when the blade failed in the base material and inside of the 99% prediction interval on the stress versus cycles to failure plot. Although this is a good sign that the blade passed the fatigue test, having the other ten blades fail either outside of this prediction interval or in the deposited material was not a promising result. Overall, this repair process was decided to be ineffective in the

current state for making complex repairs to IBR blades that would allow for the parts to

return to operation.

5 Powder DED Results

In this chapter, the laser blown powder directed energy deposition (LBP-DED) repairs are discussed in regard to the CT pore analysis and fatigue testing results. A total of 17 blades were repaired from rotors A, B, and C using varying sets of processing parameters aimed to produce different results. The blades were also CT scanned and analyzed to locate large pores in the deposited material that may cause concern for decrease in mechanical performance. Post-failure analysis was completed after cracks were formed in the blades during vibration fatigue testing. Any additional details for the LBP-DED process are also discussed that allow direct comparisons to be made to the wire DED process.

5.1 Repair Process

Similar to the wire DED process, the LBP-DED process melts Ti-6Al-4V alloy material to the surface of a component using a 1kW fiber laser. Both the laser and powder feeder move along the surface of the part to simultaneously blow powder into the specified area and melt the particles to the surface. This process can be generally described using Figure 24. The diagram shows the orientation of the laser and powder feeder, along with the formation of the material on the substrate. The process is run in an argon controlled chamber to prevent oxidation issues from occurring during the build. During the melting process, the laser was pulsing rapidly to prevent the part from overheating. Leaving the laser on the entire time could have caused the part to become overheated and created unwanted changes to the surrounding base material microstructure. This was avoided by using the pulsing technique with the laser.
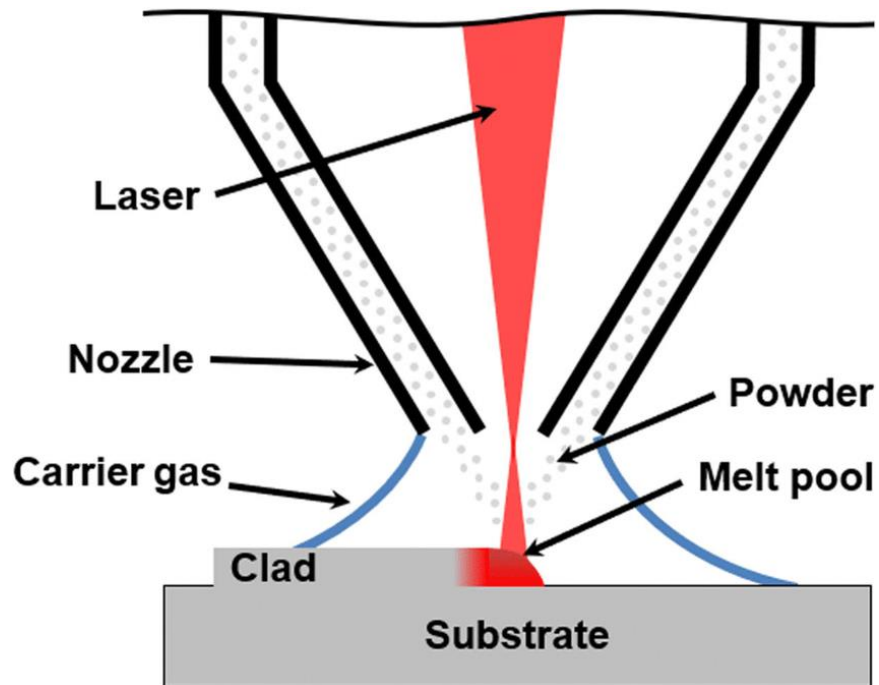
Figure 24: Diagram of the general procedure for a LBP-DED process [25]

For the blade repairs, this system started at the inner most portion of the removed section and worked outwards, blowing powder into the gap, and adding one layer at a time. These layers were purposefully built larger than the blade to fill as much of the removed portion as possible, then the repaired area was hand polished back to nominal geometry afterwards. An example of the final deposit from a leading edge repair can be seen in Figure 25.

A total of 17 blades were repaired using the LBP-DED process from three different rotors, referred to as A, B, and C. The repairs that were completed on blades from rotors A and B were repaired individually, similarly to the wire DED repairs. Rotor C blades, however, were repaired while still attached to the hub of the IBR. To account for the changes that were required when repairing IBR blades that were still intact, a power table was developed by the repair company that aimed to make dynamic changes to the amount of energy being used to create the repair based on the thickness of blade at any given point. This power table was created by the repair developers and remains proprietary to the business. The goal of the power table was to prevent too much power in the thinner portions and to also increase power along the edges of the repair area for better melting.

5.2 Pore Size Distributions

Data collection and analysis of the pores found in the repairs was compiled into pore distributions that showed which repair process was more effective and consistent. For comparison purposes, three ranges of pore diameter sizes were created to qualify each repair. These three size ranges were 100 µm, 131 µm, and 227 µm, going from best to worst. Acceptable repairs contained pores that were less than the 227 µm threshold, any pores over this size were not desirable. Statistics that represent the number of pores in each category of sizes can be seen in Table 3. Figure 26 is a probability density function (PDF) and Figure 27 is a cumulative distribution function (CDF) obtained through CT analysis of the internal pore distribution. The PDF graph shows the probability of different pore sizes being found in each of the blown powder repairs. For this PDF to be created, all visible pores had to be measured to give an accurate representation of the probability for each pore size in each individual repair. Rotors A and B, which were repaired individually, have a small grouping of peaks in the curves right around 100 µm as the most probable pore size. This means that many of the pores that are going to be found in those repairs will be less than or equal to this 100 µm value threshold. On the contrary, there are still pores being measured in most of the repairs that are larger than this threshold. While more focus is spent on the pores that are greater than this 100 µm size, it is encouraging to see some of the repairs be more centralized around this 100 µm pore size.

Blade #	Repair Location	Largest Pore Diameter (µm)	# of Pores	% > 227	% > 131	% > 100
A-3	TE	141	42	0.0%	2.4%	26.2%
A-6	LE	189	26	0.0%	7.7%	11.5%
A-7	TE	126	27	0.0%	0.0%	11.1%
A-16	LE	152	80	0.0%	1.3%	12.5%
A-19	LE	89	6	0.0%	0.0%	0.0%
B-9	LE	141	58	0.0%	0.0%	5.2%
B-11	LE	141	11	0.0%	9.1%	18.2%
B-13	TE	120	15	0.0%	0.0%	6.7%
B-14	TE	152	128	0.0%	2.3%	8.6%
C-5	LE	226	86	0.0%	7.0%	8.1%
C-6	LE	288	17	11.8%	17.6%	17.6%
C-7	TE	120	4	0.0%	0.0%	25.0%
C-13	LE	441	35	11.4%	14.3%	17.1%
C-15	TE	189	5	0.0%	20.0%	20.0%
C-17	LE	353	71	4.2%	14.1%	16.9%
C-19	TE	144	15	0.0%	13.3%	20.0%
C-21	TE	227	36	2.8%	2.8%	2.8%

Table 3: CT pore measurement results for the LBP-DED repairs

The one exception from rotor A that has the large spike on the graph is due to an extremely small number of pores that were found in the repair section of blade A-5, also seen in Table 3. Rotor C blades are shown by the curves that are flatter and wider due to the different repair procedure. This rotor has larger maximum pores and more pores overall, resulting in an overall larger range of pore sizes. This conclusion can also be made when looking at the CDF graph, which shows the probability of a pore being smaller than a given value. The lines on this graph appear to approach a value of one on the y-axis when the pores reach the maximum size for each individual repair, meaning there is a very high probability that a pore will be less than that size. It should be noted that these larger pores that were found in rotor C were found near the repair line. These lack-of-fusion pores were

created in the repair when the laser would have to turn around at the edge of the repair section.
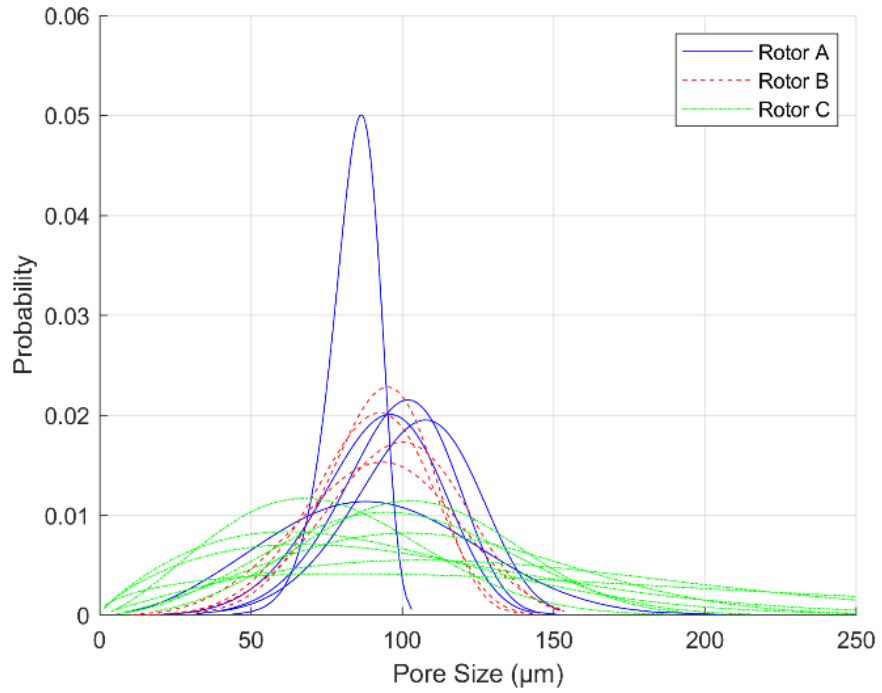

Figure 26: Probability density function for pore diameters of each individual LBP-DED repair from Rotors A, B, and C

The mean value, standard deviation and maximum feret diameter for the pores that were found in each of the repairs are shown in Figure 28. The mean value shows the average pore size for each repair that was completed. This mean is desired to be less than 100 µm, and in most cases for rotors A and B, as well as for a few blades in rotor C, this was true. It is known that not all the pores were under 100 µm for these rotors. If this were the case, then the mean would be much lower, and the range of pore size probability would be contained to less than 100 µm. As is shown in the PDF in, as well as the max diameter plot in Figure 28, this is not the case since the range of pore probability covers diameter sizes over 250 µm. However, a mean that is less than 100 µm and a max value less than 227 µm is approaching the acceptable range. In rotor C, it is shown that there are higher mean values for half of these rotor blades due to the large range of pore sizes and large maximum pore sizes. The error bars on the mean value plot represent the standard deviation on pore size that was measured for each repair. These standard deviations ranges become much larger with the repairs completed on rotor C, further displaying that these repairs were not as successful as the other two rotors which have a tighter range for standard deviation. The initial repair process was successful for rotors A and B since the max pore size was less than 227 µm in all nine repairs, with three being below the 131 µm range and one repair having a max pore size of just 89 µm. The large pores that were found in some of the repairs would need to be reduced or completely removed to consider that repair process successful.
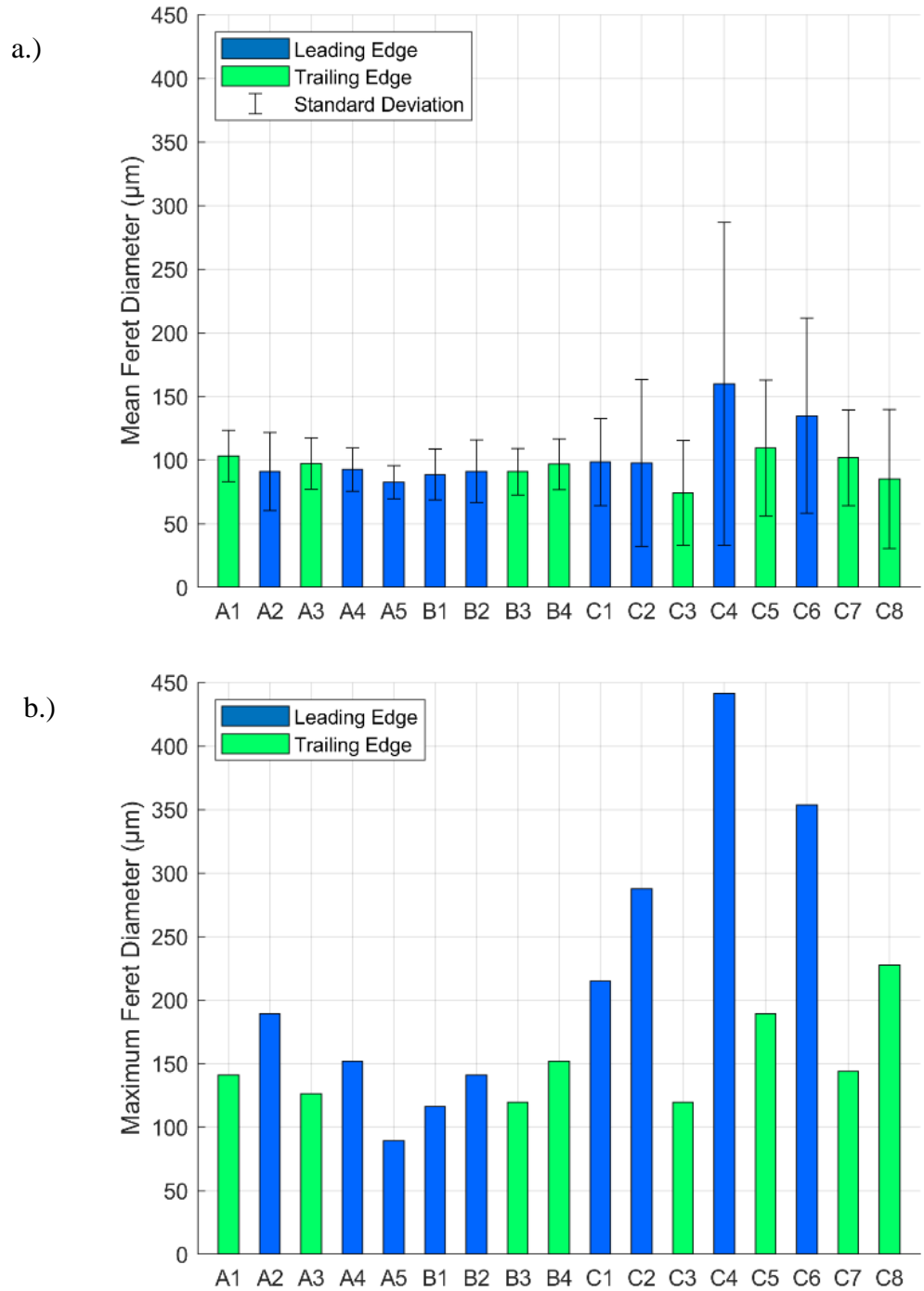
Figure 28: a.) Mean value of the pore size across each individual repair from Rotors A, B, and C with error bars representing the standard deviation of pore sizes for each repair, and b.) max feret diameter found for a single pore in each repair

65

5.3 Fatigue Testing Results

To establish a baseline, a group of 16 blades with no repairs were tested with the vibration bending set up to determine the expected life from blades that have not been altered since operating in the field. From these baseline blades, it was determined that the typical failure point on this type of blade occurred at the root, near the trailing edge where a fillet occurs that transitions from the airfoil to the base of the blade. Figure 29 represents the results from the tests for the stress versus cycles to failure for all the blown powder repairs and baseline data and the solid black line is a 99% prediction interval that was created from baseline data that was collected when testing engine blades from the same rotors that had not been repaired via DED. The repaired blades that were tested are shown for rotor A and B in the blue and purple markers. The repair data is still mostly within the range of the 99% prediction interval that was created using baseline data. Of the three repairs that ended up outside of the prediction, only blade A-5 failed in the repaired section. There were two blades that failed in the base material of the blade but outside of the range of the prediction interval. This is expected to be due to the condition of the blades when received before any work had been done for this project since there was previous use for each of these rotors in engines.
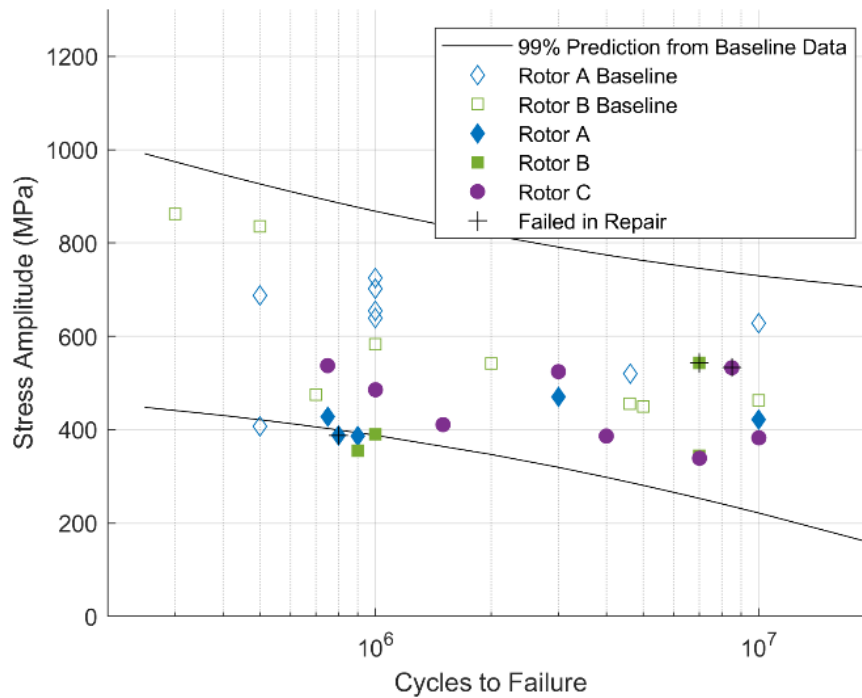
Figure 29: Stress versus Number of Cycles to Failure from vibration fatigue testing for each individual blade in Rotors A, B, and C.

Table 4 shows all the results from the tests that were completed. All blades except for three failed in the base material, not in the deposited repair material that was added. The typical location of failure in the base material was at the root of the blade near the trailing edge, right along the fillet curvature that combines the blade with the base. This location was the maximum stress point in the blade during the previous duty cycles that each of these rotors endured. When in engine operation, these blades experienced sweeps through multiple modes of vibration, thus creating stress at the root of the blade as the cycles were accruing. These duty cycles are accumulated at many different speeds depending on the rotor, giving each individual blade a varying number of cycles that falls within a large range. Knowing that this type of stress was applied previously, along with the root having the highest stress in mode two, explains why the blades tended to fail at this common location.

Two of the three blades that cracked in the deposited material were the highest stress values at failure that were recorded for any of the 17 blades tested. A reasonable explanation for why this happened with these two blades could be related to the duty cycles as well. If these two blades had low response to the cycle accumulation during engine operation, there is a chance that the blades had a very long life left when repaired. A longer operation life explains why these two had the highest failure strain since the common failure point had not accumulated enough cycles to cause failure just yet. Had the other 14 blades experienced the same number of previous cycles during engine operation, they too may have failed at higher strains in the repaired areas. The lower acquisition of duty cycles may have caused the unrepaired section of these blades to be even more resilient to the fatigue tests, thus making the repair area the new weakest section of the blade.

Blade #	Repair Location	Failure Location	Cycles per Step of Test	Failure Strain (με)	Failure Stress (MPa)
A-3	TE	Root, in base material	750,000	3,300	427.62
A-6	LE	Root, in base material	3,000,000	3,600	470.72
A-7	TE	Root, in base material	10,000,000	3,300	421.42
A-16	LE	Root, in base material	900,000	3,300	387.01
A-19	LE	On LE, in repair	800,000	2,875	387.27
B-9	LE	Root, in base material	900,000	2,700	355.49
B-11	LE	Root, in base material	7,000,000	3,000	542.58
B-13	TE	Middle, in repair	1,000,000	4,500	389.89
B-14	TE	Root, in base material	7,000,000	3,300	343.71
C-5	LE	Root, in base material	1,000,000	3,900	485.73
C-6	LE	Middle, away from repair	750,000	4,300	537.36
C-7	TE	Root, in base material	3,000,000	4,500	524.52
C-13	LE	Root, in base material	10,000,000	3,000	382.64
C-15	TE	Root, in base material	7,000,000	3,000	338.97
C-17	LE	Root, in base material	4,000,000	3,300	386.53
C-19	TE	Root, in base material	1,500,000	3,600	410.95
C-21	TE	Middle, in repair	8,500,000	4,500	532.88

Table 4: Fatigue testing results from LBP-DED repaired blades testing of each individual repair from Rotors A, B, and C

Of the three deposited material failures, A-19, B-13 and C-21, the only fracture surface where a pore was found in the initiation site of the failure was blade B-3. There were no pores that were visible at the initiation site on the fracture surface of blades A-19 or C-21 using both an optical and a scanning electron microscope, but there was one small pore at the initiation site of the fracture surface for blade B-13. This was found to be a gas pore with a diameter of approximately 41 µm. Figure 30 shows both the CT scan image and the image taken using an optical microscope of the pore found at the initiation site. This is interesting because the initiation point at a 41 µm pore was not expected when there was a 120 µm pore also in the same repair, therefore further investigation was required and is discussed in the following sections.

a)
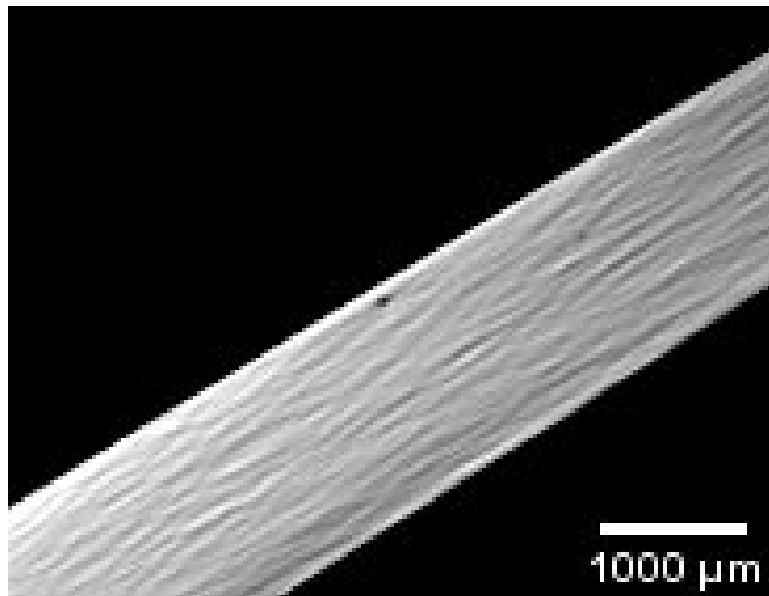
b)
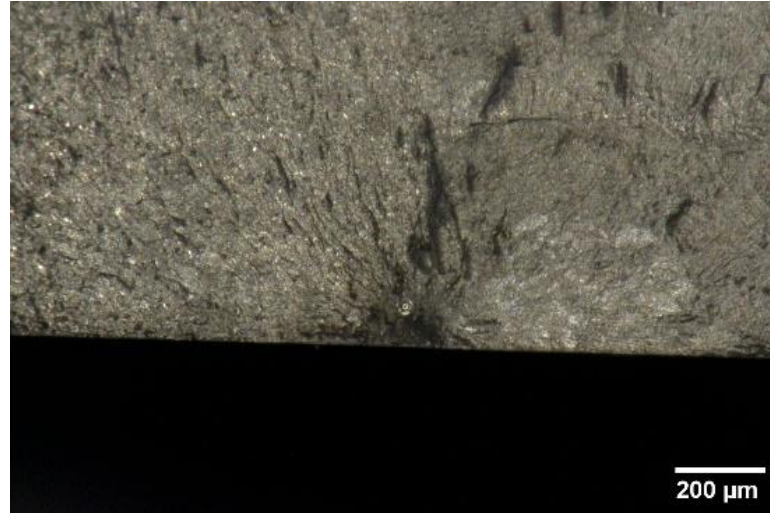
Figure 30: Initiation pore for blade B-3 in a) a CT scan and b) an optical microscope image.

The premature failure that is shown in the table for blade A-19, this being the only blade that failed outside of the 99% prediction interval created using the baseline material, is most likely due to a combination of the surface condition after being hand polished to nominal geometry and previous duty cycles, as mentioned previously. The fracture surface for this blade was damaged during the testing procedure and in attempt to separate the blade for fracture analysis to the point where an initiation point could not be fully determined. However, this crack does appear very close to the base of the blade and spans both the deposited material and the base material. Figure 31 shows this crack from blade A-19 in relation to the base of the blade. Although the fracture surface of this blade does have the striation marks that are typically associated with pointing towards the point of initiation, this blade does not have one point that can be determined. The crack did occur near the base, which would have been at the very bottom of the repair, meaning a majority of this crack was spread through the base material. There is a chance that the crack initiated in the base material and spread to the leading edge as shown in the image.

70

Figure 31: Crack in blade A-19 that spreads from LE to base material of blade outside of the repair

5.4 Fracture Surfaces

Figure 32 shows fracture surfaces of some of the other repaired blades as a comparison to see what the typical initiation sites look like. These are blades A-3, B-4, and C-5, and each of these failures occurred at the max stress location near the root of the blade. The initiation point for each of these examples points towards the surface of the blade where the max stress is depicted in Figure 16, which is represented by the center of all the striation lines that point towards the bottom middle of the fracture surface in each image. Every blade that was tested, both baseline and repaired blades, failed at this point with a similar initiation to the images being shown below. These fractures surfaces are examples of what the typical failure for these tests is expected to look like.
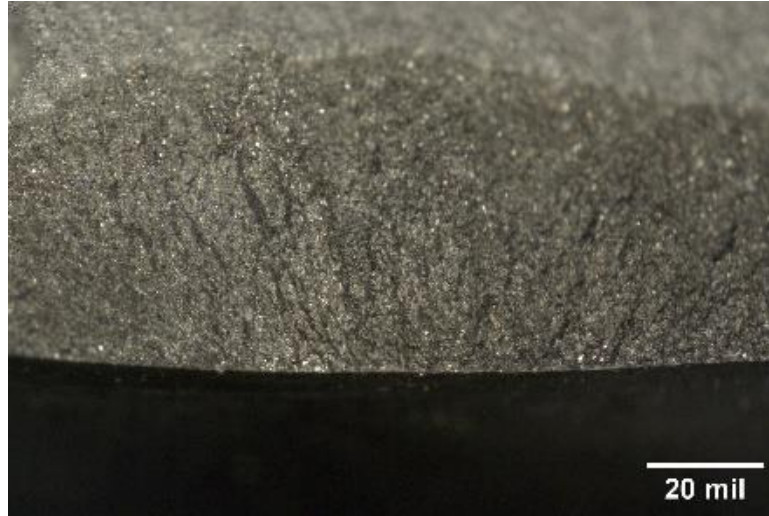
Figure 32: Initiation point on the fracture surface of blade a.) A-3, b.) B-4, and c.) C-5.

5.5 Conclusions

The LBP-DED process results were given based on CT scans and fatigue testing. Repairs were completed on 17 blades from three different rotors, with the rotor C repairs occurring while the blades were stilled attached to the hub of the IBR. The biggest take away from these repairs is that only one blade out of 17 failed in the deposited material and outside of the 99% prediction interval. The other blades that failed in the repair area did fall into the prediction range, falling in line with the un-repaired baseline data and making it a successful fatigue test. Continuing to tune this repair process and reduce the number of and overall size of the pores in the repair area will make this one step closer to becoming a viable repair process.

6 Extended Powder DED Analysis

This chapter is a continuation of the results and discussion of the LBP-DED repairs, with more emphasis on determining the reason for the few failures that occurred on the repaired portion of the blade. Discovering the cause for these types of repair failures in the fatigue testing environment would provide a great deal of insight into the changes that need to be made for a process such as this to become widely used for IBR repairs. The chapter discusses the effects of the stress distribution on the location of the pores, and how this may be able to be used in the future for fatigue life predictions on similar repairs.

6.1 Fatigue Testing Stress Distribution

The typical failure point on this type of blade occurs at the root, near the trailing edge where a fillet occurs that transitions from the airfoil to the base of the blade. This failure point is expected because the maximum stress being located at this location for this type of blade testing based on the FEA results. Figure 16 shows the stress contour plot of the blade after an FEA analysis that simulated the shaker testing where the blade is clamped at the base and vibrated at the frequency that targets the second mode of bending. Figure 16 shows two regions of high stress for this mode shape, one as described before at the root, and one in the center of the blade that is closer to the tip. The region in the center is a result of the second node line where almost no displacement occurs due to the mode two bending shape. This node line causes increased stress as a result of low displacement in that region, but the stress is not larger than the max stress location at the root. The AM repairs were completed near this second location of high stress at the center of the blade to

determine whether pores within the AM repair could dominate over the highest stress location that is located at the root of the blade.

6.2 Pore Based Fatigue Life Prediction

The CT information was used in tandem with the results from a vibration testing method that represented the stresses a blade of this type would experience during second bend mode while operating in an engine [19]. Grouping these data sets together allowed for stress intensity factor (SIF) calculations to be completed. The calculations established a better understanding of the causes of failure in some of the repairs that cracked away from the typical failure location. After testing was completed, the stress distribution from the FEA models was used for SIF calculations that required the stress value at the location of the significant pores found to be potential causes of failure. Significant pores were those that were both large and/or located in higher stress areas. These location specific stresses were found by taking various measurements of the pore locations within the blade using the CT scans and correlating the measurements to stress values from the FEA model. This technique provided an accurate estimate of the stress value at the location for each significant pore that was then used along with the pore size measurement for SIF calculations.

Figure 33 is a modified Kitagawa Takahashi diagram [26] showing infinite life prediction as well as finite life prediction using the El Haddad model [27]. As the legend describes, the solid curve represents the Kitagawa Takahashi model, and the dashed curves represent the El Haddad model that incorporates three different limits of cycles to failure. Each of these three curves were plotted using the El Haddad model, represented by the equation

75

$$\Delta\sigma_w = \Delta\sigma_e \sqrt{\frac{l_0}{l+l_0}} \qquad (2)$$

where $\Delta\sigma_w$ is the fatigue stress limit of a component containing a crack, $\Delta\sigma_e$ is the fatigue stress limit of the component with no cracks, l is the length of the crack, and l_0 is representing the critical crack length found using the El Haddad parameter. This parameter equation is given by

$$l_0 = \left(\frac{\Delta K_{th}}{Y\Delta\sigma_e}\right)^2 \frac{1}{\pi} \qquad (3)$$

where ΔK_{th} is the SIF threshold and Y is the SIF shape factor value.

The three El Haddad curves show the allowable stress amplitude to achieve the 2.5e5, 1e6, and 1e7 cycles that were chosen for comparison purposes. The green, yellow, and red vertical lines that have been added to the graph represent failure from a 100 µm, 131 µm or 227 µm pore, respectively. Each line was found by drawing a straight horizontal line from the interception of the y-axis of the graph until it intercepted the Kitagawa Takahashi line, then drawing a vertical line straight down until it intercepted the x-axis. The green line was chosen to represent the pore size threshold that is safe to operate under for the fatigue performance of the repaired blade to fall within the same range as the baseline data. When the pore size starts to approach the ranges beyond this value, specifically higher than the 227 µm threshold, this is where the fatigue performance begins to significantly deteriorate. The goal overall was to understand the consequences of having pores larger than these thresholds on the blade performance, as well as seeing how the experimental limits of pore size would compare to this model.
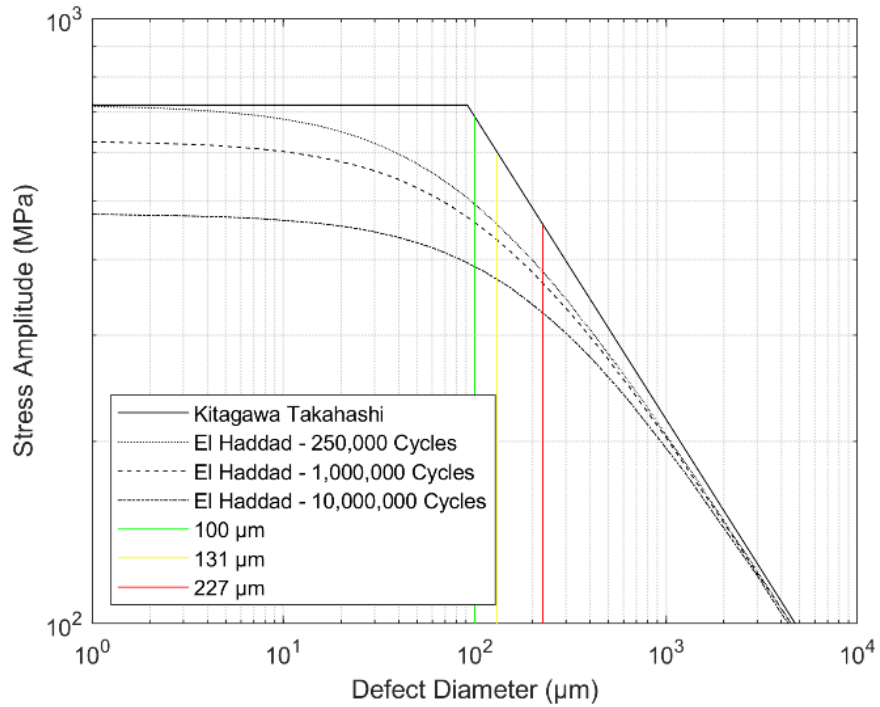
Figure 33: Kitagawa-Takahashi diagram with El Haddad Curves. The green line represents failure from a 100 µm pore, the yellow line is 131 µm, and the red line is 227 µm.

6.3 Analysis of Failure at Pores

The initiation point for blade B-3 was found to be a small pore using fractography on an optical microscope, as shown in Figure 30. The pore was measured on the fracture surface to be 41 µm in diameter. This was confirmed by locating and measuring the pore in the CT images. Since the voxel size of the CT scan was only 28 µm, this pore was very hard to detect on the CT scan as it only appeared to be about 1 to 1 1/2 pixels in size. Figure 30 shows the images from the CT scan and the optical microscope of the initiation pore. A pore of this size is surprising to see as initiation point in a repair section of a blade with other pores being found in the same repair that were found to be three times the size of this one. To further explain why this small pore caused failure, SIF values were considered.

Using the FEA stress distribution, specific stress values at the locations of the pores were obtained. The pore locations were found using measurements from the CT images. Using these location measurements, the closest node in the FEA model was located and the uniaxial stress at this specific pore location was measured. This stress value, representing the stress at the pore location from the FEA model, was then compared to the max stress from the FEA model to get a percentage of max stress. The max stress in the FEA model was in the same location as the max stress for the blade during a mode two vibration test, therefore the max stress from the model can be taken as equal to the failure stress that was calculated based off the strain of the final step for each blade. Doing this allows for a percentage of failure stress to be calculated for each pore location, which was then used for the SIF calculations that are shown below in Table 5.

Pore #	Df (μm)	eo (μm)	A (μm²)	(√A) /e0	σ (MPa)	K (MPa√m)
1	119.674	621.836	5568.654	0.12	177.47	1.358288773
2	101.707	382.714	4773.132	0.18	427.03	5.683337568
3	101.707	378.398	4773.132	0.18	491.99	6.475516233
4	40.000	132.705	1591.044	0.30	508.95	5.228961843

Table 5: SIF Calculations for top 3 pores and the initiation pore. Df = pore diameter, eo = distance to the free edge of the blade

Focusing on specific pores was required to have a good comparison between multiple repairs and the gas pore that was found in the initiation cite of blade B-3. This gas pore was located on the FEA model, as shown in Figure 34. Using the pore size that was measured in the CT scan and these stress values at the locations of the pores, SIFs for various pores were calculated. The SIF showed the significance of the stress at specific locations associated with the pore size. The SIF was calculated using the equation

$$\Delta K_I = Y\sigma \sqrt{\pi \sqrt{A_i}} \qquad (4)$$

78

that includes the size of the pore (A_i), a shape factor that represents the depth of the pore from the surface (Y) and the stress at that location of the pore (σ) [49, 50]. The shape factor in the equation can have a different value if the size of the pore in relation to the distance it is from the surface exceeds a value of 0.8. This value is shown as A_i/e_0, along with the other results, in column five Table 5. The results of these calculations show that the SIF can be a larger value for a smaller void if the stress around the smaller void is higher than the stress around the larger void. However, the maximum SIF value here is not the pore that caused failure. The crack most likely initiated at pore number four due to the distance from the surface, e_0, being much smaller. Although this distance is smaller, it is not small enough to give a value less than 0.8 in column five of Table 5, which would require a change in the shape factor for Equation 4. The value that was used for Y in all these calculations was 0.5, but this value would increase to 0.65 if A_i/e_0 was greater than 0.8, thus increasing the overall SIF.

In Equation 4, it is shown that the stress has a larger effect than the area of the pore when finding the value of the SIF. This means that the stress would not need to be that much larger for a smaller void for it to have a larger SIF than that of a larger void with a smaller stress. Notice in Figure 34 that the location of the pore that initiated failure is very near the area of maximum principal strain. This further explains why the gas pore caused initiation even though it was much smaller than the largest pore found in the repair section, and this was due to the high stress it was experiencing.
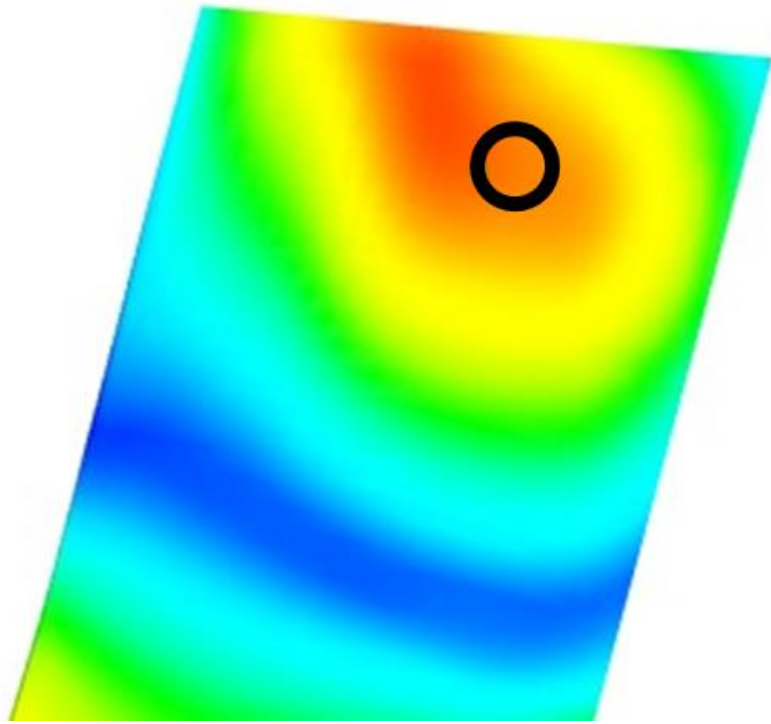
Figure 34: Maximum principal strain plot of blade in mode two vibration simulation using FEA with black circle representing the location of the gas pore that was found on the fracture surface of blade B-3.

7 Conclusions

Two DED processes were used to repair 28 IBR blades that endured rigorous vibration testing with advantageous results. CT scans were used to detect pores larger than the 100 µm threshold that needs to be analyzed to confirm the validity of the repair, according to the Kitagawa Takahashi Diagram. This process provided important information that can be used in the future to help provide a level of prediction when it comes to fatigue life of a component that contains pores. Blades that were repaired using the wire DED process may not have performed to the standard that was required to make the repairs successful, but it was a great source of information on how larger voids in the material can affect the performance of such a complex component. For almost all the LBP-DED repaired blades in rotors A and B, and as well as some blades from rotor C, the mean pore size was under 100 µm. This is a step in the right direction of achieving the goal to have all pores in the repair be less than 100 µm, even though only one of these repairs had a maximum pore size be less than this value.

Overall, the LBP-DED repairs were successful as the two failures in the repair sections occurred at very high strains and the one that failed outside of the interval was most likely due to previous operation that shortened the fatigue life. All but two of the failures that occurred in the base material fell within the prediction interval that was created with the baseline blade data. Again, this was most likely due to previous duty cycles since the repair had no change on the failure location and fatigue life for these two blades to cause failure outside of the prediction interval. If these blades were in pristine condition before the repair process was started, it could be expected to see many of the blades to

perform exactly like the baseline data that was found previously with no repairs. Therefore, this LBP-DED process is validated as a viable option for turbine engine blade repairs that has the potential to save significant amounts of time and money in the future.

7.1 Future work

This work that has been completed has put a large focus on finding a potential repair technique for the IBR type blades that are damaged in operation. However, the technique that has been found, as well as the evaluations of the parts being conducted, have room for improvement. Refining the DED repair process to further eliminate the production of pores, thus increasing the potential life for a repaired specimen, is the main goal for this line of work moving forward. Doing so would relieve any concerns about adding defects that will cause failure in a part when the goal was to try to repair the part in the first place.

Characterizing these pores along the way is also very important. Improving the strategies used to locate and measure the number of defects found in these repairs is crucial in understanding how the pores were formed and what can be changed to avoid the creation of the pores. Techniques such as CT scans have limited capabilities for larger parts, so there will most likely be some sort of process developed that incorporates another technique into this procedure to be used alongside the CT scanning technique. Current recommendations for other techniques to be used are NDE types, such as ultrasonic testing or X-ray scanning.

Optimizing the methods used to complete this work will hopefully allow for implementation of the procedure on larger IBR specimens in the future. Creating a repair process that is viable for many IBR shapes and sizes would be a significant improvement

to the current repair or replace process that is used for IBR failure. Eventually, the criteria

could be met to allow for these types of repairs to take place on IBRs that will return to the

field of operation and continue to save time, money, and resources for the groups involved

in the manufacturing of new IBR parts.

References

[1]   O. Scott-Emuakpor, D. Gillaugh, B. Runyon, L. Smith and P. Johnson, "Refinement of a High Cycle Fatigue Decision-Gate Assessment for Additively Repaired Blades," in *ASME/Turbo Expo*, Rotterdam, 2022.

[2]   B. Denkena, V. Boess, D. Nespor, F. Floeter and F. Rust, "Engine blade regeneration: a literature review on common technologies in terms of machining," *The International Journal of Advanced Manufacturing Technology,* pp. 917-924, 2015.

[3]   A. L. Gyekenyesi, "CHARACTERIZATION OF A WIRE FEED DIRECTED ENERGY DEPOSITION," 2020.

[4]   R. Kragseth, "Thermal Processes for Additive Manufacturing," 4 June 2021. [Online]. Available: https://www.process-heating.com/articles/93694-thermal-processes-for-additive-manufacturing.

[5]   P. Kattire, S. S. R. Paul and W. Yan, "Experimental characterization of laser cladding of CPM 9V on H13 tool steel for die repair applications," *Journal of Manufacturing Processes,* vol. 20, pp. 492-499, 2015.

[6]   L. P. Borrego, J. T. B. Pires, J. M. Costa and J. M. Ferreira, "Mould steels repaired by laser welding," *Engineering Failure Analysis,* vol. 16, no. 2, pp. 596-607, 2009.

[7]   H. Koehler, K. S. T. Partes and F. Vollertsen, "Laser reconditioning of crankshafts: From lab to application," *Physics Procedia,* vol. 5, pp. 387-397, 2010.

[8]   R. P. Mudge and N. R. Wald, "Laser engineered net shaping advances additive manufacturing and repair," *Welding Journal New York,* vol. 86, no. 1, p. 44, 2007.

[9]   J. M. Wilson, C. Piya, Y. C. Shin, F. Zhao and K. Ramani, "Remanufacturing of turbine blades by laser direct deposition with its energy and environmental impact analysis," *Journal of Cleaner Production,* vol. 80, pp. 170-178, 2014.

[10]   W. J. L. W. J. K. M. S. J. J. B. &. S. D. S. Oh, "Repairing additive-manufactured 316L stainless steel using direct energy deposition," *Optics & Laser Technology 117,* pp. 6-17, 2019.

[11]   B. Germann, "Directed Energy Deposition for Repair of Industrial Components: How 3D Metal Printing Saves Time and Lowers Costs," 12 March 2019. [Online]. Available: https://optomec.com/how-3d-metal-printing-saves-time-and-lowers-costs-ded-for-repair-of-industrial-components/.

[12]   P. Z. X. C. X. S. H. M. H. &. L. Y. Zhang, "Elucidation of bubble evolution and defect formation in directed energy deposition based on direct observation," *Additive Manufacturing,* p. 101026, 2020.

[13]   A. M. Vildanov, K. D. Babkin and E. V. Alekseeva, "Macro defects in direct laser deposition process," *Materials Today: Proceedings,* vol. 30, no. 3, pp. 523-527, 2020.

[14]   Z. Liu, B. He, T. Lyu and Y. Zou, " A review on additive manufacturing of titanium alloys for aerospace applications: directed energy deposition and beyond Ti-6Al-4V," *JOM,* vol. 73, pp. 1804-1818, 2021.

[15]   A. Lopez, "Non-destructive testing application of radiography and ultrasound for wire," *Additive Manufacturing,* pp. 298-306, 2018.

[16]   N. Tapoglou and J. Clulow, "Investigation of hybrid manufacturing of stainless steel 316L components using direct energy deposition," *Proceedings of the Institution of Mechanical Engineers, Part B: Journal of Engineering Manufacture,* pp. 1633-1643, 2021.

[17]   S. Kersten, M. Praniewicz, T. Kurfess and C. Saldana, "Build orientation effects on mechanical properties of 316SS components produced by directed energy deposition," *Procedia Manufacturing,* pp. 730-736, 2020.

[18]   X. Zhang, W. Shen, V. Suresh, J. Hamilton, L. H. Yeh, X. Jiang and H. Qin, "In situ monitoring of direct energy deposition via structured light

system and its application in remanufacturing industry," *The International Journal of Advanced Manufacturing Technology,* pp. 959-974, 2021.

[19]   O. Scott-Emuakpor, "Investigating Discrepancies in Vibration Bending Fatigue Behavior of Additively Manufactured Titanium 6Al-4V," *Journal of Engineering Materials and Technology,* 2019.

[20]   L. Sheridan, "Stress-defect-life interactions of fatigued additively manufactured alloy 718," *International Journal of Fatigue,* 2021.

[21]   S. Romano, A. Brückner-Foit, A. Brandão, J. Gumpinger, T. Ghidini and S. Beretta, "Fatigue properties of AlSi10Mg obtained by additive manufacturing: Defect-based modelling and prediction of fatigue strength," *Engineering Fracture Mechanics,* vol. 187, pp. 165-189, 2018.

[22]   H. Chen, Y. Yang, S. Cao, K. Gao, S. Xu, Y. Li and R. Zhang, "Fatigue life prediction of aluminum alloy 6061 based on defects analysis," *International Journal of Fatigue,* vol. 147, p. 106189, 2021.

[23]   J. Schindelin, I. Arganda-Carreras, E. Frise, V. Kaynig, M. Longair, T. Pietzsch and A. Cardona, "Fiji: an open-source platform for biological-image analysis," *Nature Methods,* pp. 676-682, 2012.

[24]   J. L. Dávila, P. I. Neto, P. Y. Noritomi, R. T. Coelho and J. V. L. da Silva, "Hybrid manufacturing: a review of the synergy between directed

energy deposition and subtractive processes," *The International Journal of Advanced Manufacturing Technology,* pp. 3377-3390, 2020.

[25]   J. Dill, M. Soshi and K. Yamazaki, "A study on the effect of directed energy deposition substrate energy on clad geometry," *The International Journal of Advanced Manufacturing Technology,* pp. 315-333, 2020.

[26]   H. Kitagawa and S. Takahashi, "Applicability of fracture mechanics to very small cracks or the cracks in the early stages," *Proceedings of Second International Conference on Mechanical Behavior of Materials,* pp. 627-631, 1976.

[27]   M. El Haddad, T. Topper and a. S. K.N., "Prediction of non propagating cracks," *Engineering Fracture Mechanics,* pp. 573-584, 1979.

[28]   X. Huang, "Wide Gap Braze Repair of Gas Turbine Blades and Vanes—A Review," *ASME Journal of Engineering for Gas Turbine and Power,* 2011.

[29]   Y. Fomichev, "Reconditioning gas turbine blisks by electron beam welding a repair insert," *Welding International,* pp. 219-221, 2015.

[30]   R. Biswal, "Criticality of porosity defects on the fatigue performance of wire + arc additive manufactured titanium alloy," *International Journal of Fatigue,* pp. 208-217, 2019.

[31]   J. Yan, "Optimization of Multi-materials In-flight Melting in Laser Engineered Net Shaping (LENS) Process," in *Solid Freeform Fabrication Symposium*, 2014.

[32]   L. Sheridan, "Relating porosity to fatigue failure in additively manufactured alloy 718," *Materials Science and Engineering A,* 2018.

[33]   Y. Murakami and T. Endo, "Effect of small defects on the fatigue strength of metals," *International Journal of Fatigue,* pp. 23-30, 1980.

[34]   A. D. Williams and J. L. Humphries, "Latest Gas Turbine Repair Techniques Using Laser Technology," *Proceedings of the International Thermal Spray Conference,* vol. 2, pp. 1431-1435, 1998.

[35]   W. J. Oh, W. J. Lee, M. S. Kim, J. B. Jeon and D. S. Shim, "Repairing additive-manufactured 316L stainless steel using direct energy deposition," *Optics & Laser Technology 117,* pp. 6-17, 2019.

[36]   M. Wevers, B. Nicolaï, P. Verboven, R. Swennen, S. Roels, E. Verstrynge and H. Claes, "Applications of CT for non-destructive testing and materials characterization," in *Industrial X-Ray Computed Tomography*, Cham, Switzerland, Springer, 2018, pp. 267-331.

[37]   P. Zhang, X. Zhou, X. Cheng, H. Sun, H. Ma and Y. Li, "Elucidation of bubble evolution and defect formation in directed energy deposition based on direct observation," *Additive Manufacturing,* p. 101026, 2020.

[38]   N. Sanaei and A. Fatemi, "Defect-based fatigue life prediction of L-PBF additive manufactured metals," *Engineering Fracture Mechanics,* vol. 244, p. 107541, 2021.

[39]   A. Yadollahi, M. J. Mahtabi, A. Khalili, H. R. Doude and J. C. Newman Jr, "Fatigue life prediction of additively manufactured material: Effects of surface roughness, defect size, and shape.," *Fatigue & Fracture of Engineering Materials & Structures,* vol. 41, no. 7, pp. 1602-1614, 2018.

[40]   O. Scott-Emuakpor, "STRUCTURAL INTEGRITY ASSESSMENTS FOR VALIDATING DIRECTED ENERGY DEPOSITION," in *ASME Turbomachinery Technical Conference and Exposition*, 2020.

[41]   D. Miller, R. Kemnitz, R. V. Grandhi and L. C. Sheridan, "Fatigue Life Modeling and Experimental Validation of Additively Manufactured Turbine Blade with Respect to Defect Size and Location," in *AIAA SCITECH 2022 Forum*, San Diego, 2022.

[42]   T. Nicholas, High Cycle Fatigue: A Mechanics of Materials Perspective, Elsevier, 2006.

[43]   J. Bruns, A. Zearley, T. George, O. Scott-Emuakpor and C. Holycross, "Vibration-based bending fatigue of a hybrid insert-plate system," *Experimental Mechanics,* pp. 1067-1080, 2015.

90

[44]   O. E. Scott-Emuakpor, H. Shen, T. George and C. Cross, "An energy-based uniaxial fatigue life prediction method for commonly used gas turbine engine materials," *Journal of engineering for gas turbines and power,* 2008.

[45]   O. Scott-Emuakpor, J. Schwartz, T. George, C. Holycross, C. Cross and J. Slater, "Bending Fatigue Life Characterization of Direct Metal Laser Sintering Nickel Alloy 718," *Fatigue and Fracture Engineering Materials and Structures,* pp. 1105-1117, 2015.

[46]   J. Bruns, "Fatigue Crack Growth Behavior of Structures Subject to Vibratory Stresses," in *Society of Experimental Mechanics Annual Conference*, Greenville, SC, 2014.

[47]   O. Scott-Emuakpor, C. Holycross, T. George, J. Beck, J. Schwartz, M.-H. Shen and J. Slater, "Material Property Determination of Vibration Fatigued DMLS and Cold-Rolled Nickel Alloys," in *ASME/Turbo Expo*, Dusseldorf, Germany, 2014.

[48]   D. Maxwell and T. Nicholas, "A Rapid Method for Generation of a Haigh Diagram for High Cycle Fatigue," *Journal of Fatigue and Fracture Mechanics,* pp. 626-641, 1998.

[49]   R. Bellows, S. Muju and T. Nicholas, "Validation of the Step Test Method for Generating Haigh Diagrams for Ti-6Al-4V," *International Journal of Fatigue,* pp. 687-697, 1999.

[50]   O. Scott-Emuakpor, T. George, C. Cross, J. Wertz and M.-H. Shen,
"A New Distortion Energy-Based Equivalent Stress for Multiaxial Fatigue
Life Prediction," *International Journal of Non-Linear Mechanics,* pp. 29-37,
2012.